Ocean and Sea Ice SAF

Visiting Scientist Report

SAF/OSI/CDOP/KNMI/TEC/TN/168

Near Real-time Sea Ice Discrimination Using SeaWinds on QUIKSCAT

by

M. Belmonte Rivas and A. Stoffelen

(April 2008)

Table of Contents

1 Introduction

Objective

Within the frame provided by the Ocean and Sea Ice Satellite Application Facility (OSI SAF) created by European Organisation for the Exploitation of Meteorological Satellites (EUMETSAT), the Royal Netherlands Meteorological Institute (KNMI) has developed sea ice screening routines for both the ERS and ASCAT radar sensors based on probabilistic distances to empirical C-Band models for sea ice and ocean backscatter ([de Haan, 2001], [Verspeek, 2006]).

The Microwave Earth Remote Sensing group at Brigham Young University (BYU) in the United States has also developed an ice screening method for the Ku-Band SeaWinds radar sensor, which KNMI adopted initially for its own processing. Prompted by its own analyses and users queries, the KNMI decided to use an additional Sea Surface Temperature (SST) filter to prevent occasional erratic winds over sea ice surfaces. Since wind information near the ice edge is quite relevant, this document reports on renovated efforts at KNMI to develop an improved sea ice detection algorithm for SeaWinds similar to the one used for ERS and ASCAT sensors, where computed residuals to geophysical Ku-Band ice and ocean model functions are interpreted as probabilities and then combined with prior information on the sea ice state using a Bayesian discrimination algorithm to produce Near Real-Time (NRT) sea ice maps.

2 SeaWinds on QUIKSCAT

The SeaWinds instrument was launched on the QUIKSCAT platform on June 1999 onto a sun-synchronous Low Earth Orbit (LEO) with a period of 101 minutes. SeaWinds uses a rotating dish antenna with two pencil beams that sweep in a circular pattern. The antenna radiates microwave pulses at a frequency of 13.4 GHz and collects the returning backscatter over a continuous 1800 km wide swath, covering 90% of the Earth's surface in one day [Leidner, 2000]. Although the primary mission of QUIKSCAT is to acquire measurements of near-surface winds over the global oceans, other science goals include monitoring the seasonal extent of the Arctic and Antarctic ice packs and the study of changes in rain forest vegetation.

Geometry of observations

SeaWinds employs a single 1 meter parabolic antenna for the reception of horizontal and vertically polarized backscatter with incidence angles of 46 (H-pol) and 54 (V-pol) degrees. The transmitted microwave pulses are frequency chirped and the backscattered returns passed through a Fast Fourier Transform stage to provide sub-footprint range resolution cells (~25x25 km^2, called slices). Each surface resolution cell (or wind vector cell, WVC) registers a total of four backscatter measurements in sequence, two of them collected by the outer V-pol antenna and another two by the inner H-pol antenna (see Fig.1).

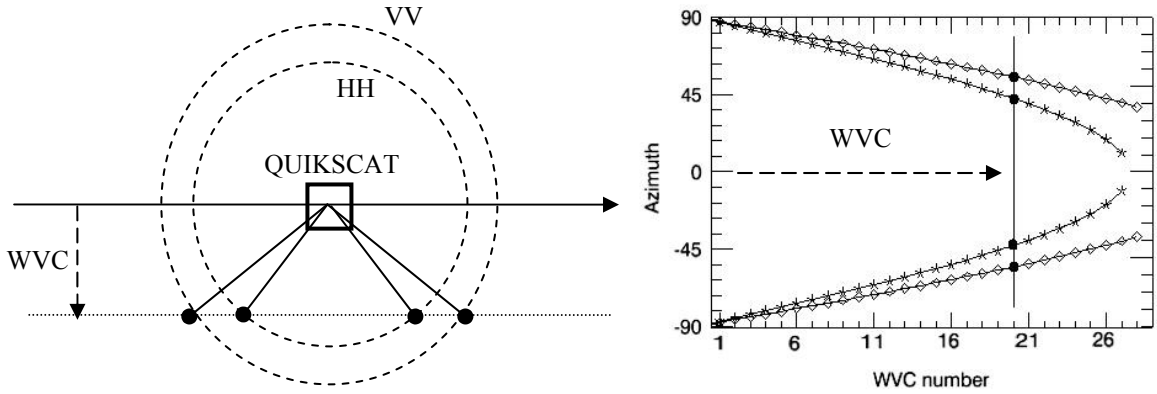

Figure 1 – QUIKSCAT provides a total of four backscatter views per resolution cell

The distance from the sub-satellite to the wind vector cell (i.e. WVC number) determines the azimuthal diversity of the measurement sequence, namely, the arrangement of viewing angles about the surface cell, which should ultimately allow for the detection of the wind direction signature over the ocean.

3 Ocean wind GMF

The empirical Ku-band ocean geophysical model function (GMF) was determined on the basis of a statistical comparison between ADEOS[1] NSCAT 14 GHz dual-polarized backscatter measurements and collocated ECMWF[2] model winds [Wentz, 1999]. The span of valid model incidence angles ranges from 15 to 65 degrees (55 degrees for H-pol) for wind speeds under 35 m/s. The most salient features of the ocean GMF (see Appendix A) are best described in terms of its own variables, namely radar incidence angle, wind speed and wind direction:

i) *incidence angle*: the observed values of ocean backscatter at both V and H polarization are equal at nadir and decrease with incidence angle, where V-pol backscatter becomes stronger than H-pol (see Fig.2). This behavior is roughly explained by the physical optics (Kirchhoff) approximation near nadir, and Bragg (resonant) scattering theory at larger incidence angles [Jones, 1977].

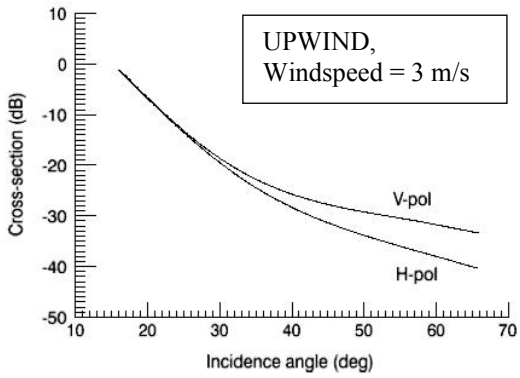

Figure 2 – Ocean backscatter vs radar incidence angle (NSCAT2)

ii) *wind speed*: The backscatter from the ocean increases with wind speed up to a point of saturation, namely, a point beyond which ocean roughness no longer responds to increasing wind speed. Theoretical studies of the ocean wave spectrum [Fernandez, 2006] indicate that the phenomenon of saturation is first initiated at small ocean length scales, spreading onto larger scales as the wind continues to increase. The saturation windspeed is thus expected to increase with radar wavelength and elevation angle (e.g. about 35 m/s for Ku-Band on QUIKSCAT).

iii) *wind direction*: ocean backscatter shows a double harmonic modulation with respect to wind direction (i.e. a small up/downwind difference with a full-cycle period in azimuth on a larger amplitude

[1] ADEOS = Advanced Earth Observing Satellite
[2] ECMWF = European Center for Medium range Weather Forecasting

half-cycle up/crosswind modulation). This azimuthal anisotropy in backscatter is strongest for moderate winds (~8 m/s) at large incidence angles (see Fig.3), and it vanishes either as windspeeds go to zero or approach the backscatter saturation point at 35 m/s.

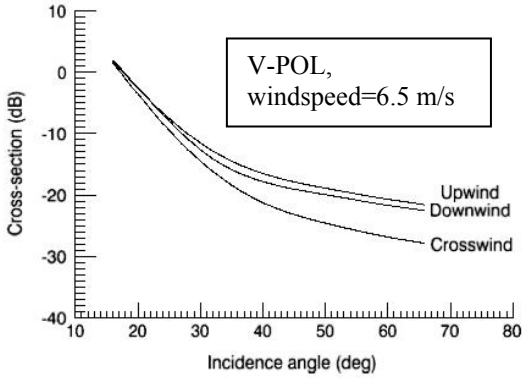

Figure 3a – Ocean backscatter vs. wind direction (NSCAT2)

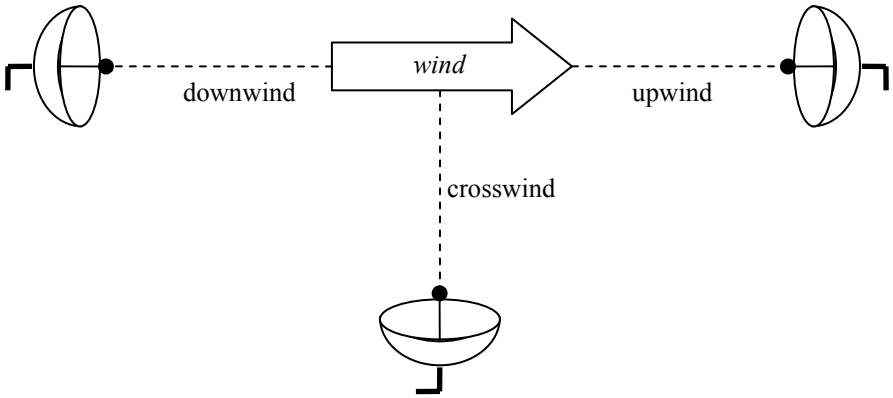

Figure 3b – Wind direction relative to transmit-receive antenna

4 Sea ice detection

In contrast to ocean wind backscatter, which is governed by surface effects, sea ice backscatter at Ku-band is mostly dominated by volume effects within the ice layer, which results in distinct polarization, intensity and directional backscatter properties that allow its effective identification against an ocean background. In particular, while ocean (surface) scattering is characterized by steep backscatter gradients relative to incidence angle and substantial polarization ratios (V/H), volume scattering from sea ice yields smaller gradients and near unity polarization ratios ([Gohin, 1994], [Yueh, 1997]). The azimuthal variability of sea ice backscatter is also much smaller than that of the ocean [Early, 1997].

4.1 BYU algorithm

The BYU sea ice detection algorithm is currently used by NOAA's National Environmental Satellite Data and Information Service (NESDIS) for the operational generation of its SeaWinds Real Time BUFR Geophysical Products. Following the same principles that have been later adopted at the Norwegian Meteorological Institute [Haarpaintner, 2004] and IFREMER [Ezraty, 2001] for the development of similar sea ice detection algorithms using SeaWinds data, the BYU algorithm capitalizes on the contrasting polarization and azimuthal modulation properties of sea ice and ocean backscatter for their effective discrimination ([Remund, 1999] and [Anderson, 2005]). Namely, the backscatter pseudo-polarization ratio (σ_V/σ_H), mean collected backscatter (σ_H), and V and H-polarized error standard deviations[1] ($\Delta\sigma_{H,V}$) form a 4-dimensional space where ocean and ice clusters become separable. In this transformed space, the BYU algorithm calculates the ice and ocean cluster centroids and covariance matrices to implement a maximum likelihood discrimination, and reduces residual misclassification noise using image processing techniques (such as region growing, erosion and dilation) to produce a binary image depicting the extent of the sea ice pack.

While it is clearly feasible to discriminate ice from open water using backscatter data during winter and calm wind conditions, the seasonal performance of a SeaWinds ice detection algorithm has not yet been exhaustively validated. Some of the problems affecting the accuracy of the BYU algorithm (see e.g. [Remund, 1998], [Remund, 2000] and [Abreu, 2002]) include:

[1] Refers to the azimuthal variability within a surface resolution cell

i) High wind events over the ocean that reduce the ice-seawater contrast, especially in areas of strong cyclonic activity such as the Greenland or Weddell Seas.

ii) Poorer discrimination over less compact (i.e. lower concentration) ice areas, such as those typical of Antarctica's sea ice margin.

iii) Summer melt effects

The resulting BYU sea ice extent estimates are nevertheless highly correlated with the NASA Team sea ice concentration edges derived from SSM/I data [Meier, 2008], as we also confirm later in Section 5 using sea ice concentrations from AMSR data (see Appendix D).

4.2 KNMI algorithm

The main difference between the BYU and KNMI sea ice detection algorithms is that the former ice and ocean cluster centroids in the 4-dimensional space of $\{\sigma^0_H , \sigma^0_V/\sigma^0_H, \Delta\sigma^0_{H,V}\}$ combinations are replaced by actual geophysical model functions for ocean and ice in the original space of SeaWinds backscatter quadruplets $\{(\sigma^0_H , \sigma^0_V)_{fore}, (\sigma^0_H , \sigma^0_V)_{aft}\}$ (Fig.4).

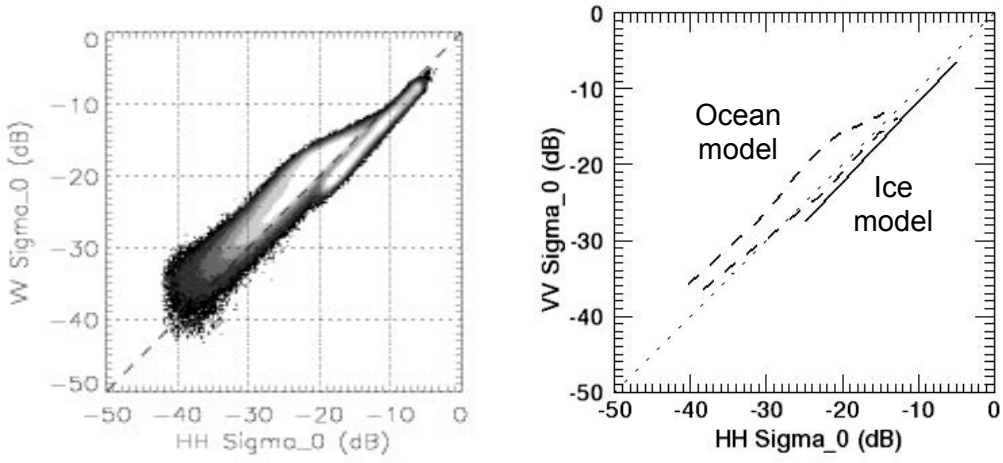

Figure 4 – Observed SeaWinds backscatter distribution (LEFT) vs. empirical model functions (RIGHT)

The KNMI algorithm computes residuals (squared distances) to pre-existing Ku-Band ocean wind and ice model functions, and the residuals are converted to probabilities after normalizing by the expected error variance about the corresponding model. These probabilities are finally combined with prior information on the sea ice state using a Bayesian approach to produce daily sea ice maps, namely:

$$p(ice \mid \sigma^0) = \frac{p(\sigma^0 \mid ice)\, p_0(ice)}{p(\sigma^0 \mid ice)\, p_0(ice) + p(\sigma^0 \mid wind)\, p_0(wind)} \qquad (1)$$

Where $p(ice|\sigma^0)$ is the conditional probability of ice given σ^0 measurements, $p(\sigma^0|ice)$ is the conditional probability of σ^0 given ice (i.e. the distribution of ice backscatter measurements about the ice model), $p(\sigma^0|wind)$ the distribution of ocean backscatter measurements about the ocean wind model, and $p_0(ice)$ is the *a priori* ice probability. Note that $p_0(wind) = 1 - p_0(ice)$, since ice and ocean are considered the only two possible outcomes in the algorithm, and that prior knowledge about the distributions of backscatter for each class is needed.

Probability distribution of ocean backscatter

The KNMI SeaWinds Data Processor (SDP, [de Kloe, 2007]) carries all the necessary information about the ocean wind GMF and its expected error variance. This information is embedded in the processor's *normalized* maximum likelihood estimator (MLE_{wind}), defined as the squared distance of measurements to the ocean GMF divided by the expected (i.e. instrumental and geophysical) noise variance [Stoffelen, 2006]:

$$MLE_{wind} = \frac{1}{\langle MLE \rangle} \sum_{i=1,\ldots,N} \frac{(\sigma^0_{obs,i} - \sigma^0_{wind,i})^2}{\mathrm{var}[\sigma^0_{wind,i}]} \qquad (2)$$

Where σ^0_{obs} is the SeaWinds observed backscatter, σ^0_{wind} is the Ku-band ocean wind GMF (i.e. NSCAT2), N is the number of independent looks available (usually four), $\mathrm{var}[\sigma^0_{wind}]$ is the instrumental noise variance [Spencer, 2000] and $\langle MLE \rangle$ is a normalization factor that accounts for deviations from the ocean wind GMF other than those related to instrumental noise (i.e. geophysical effects like sub-cell wind variability, [Portabella, 2006]). The normalized MLE_{wind} is thus constructed to guarantee that the variance of observations about the ocean wind model is unity (in linear space). Therefore, the probability to find a SeaWinds ocean backscatter quadruplet a squared distance MLE_{wind} away from the two-dimensional wind GMF surface is given by a chi-square distribution with two degrees of freedom (i.e. an exponential distribution with L = 2 [Johnson, 1994], although the exponent of the distribution is in practice adjusted to L=1.5, as in Fig.5):

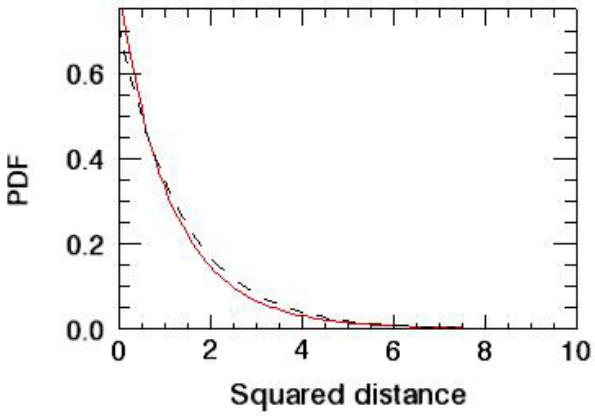

$$p(\sigma^0 \mid wind) = \frac{1}{L} e^{-MLE_{wind}/L} \qquad (3)$$

Figure 5 – Probability distribution of SeaWinds ocean backscatter about the ocean GMF: red is the observed distribution normalized to unit area, and dashed is modeled from Eq. (3) with L=1.5

Probability distribution of sea ice backscatter

To obtain the necessary statistical knowledge about the Ku-Band ice model and its error variance, we look at the actual distribution of backscatter data in the space of SeaWinds measurements. We use good quality, land-masked and rain-free backscatter measurements extracted from the NOAA/NESDIS BUFR files [Leidner, 2000], corrected for two-way atmospheric attenuation using Wentz's SSM/I rain-free climatology, and collocated with background BYU sea ice masks (Fig.6).

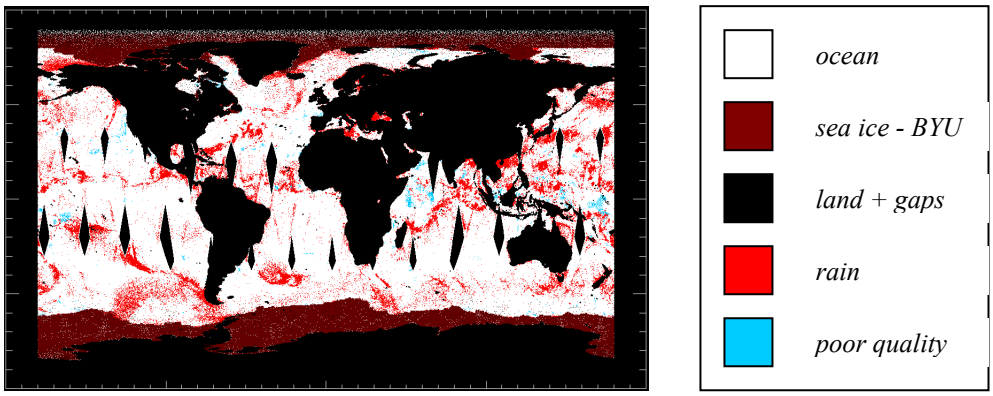

Figure 6 – Daily SeaWinds backscatter measurements

The daily distributions of sea ice backscatter data are analyzed for a period of one year, starting September 1st 2006, allowing us to draw the following conclusions:

a) Sea ice backscatter tends to cluster along a straight *ice line* on the SeaWinds 'fore' and 'aft' dB-measurement subspaces (Fig.7).

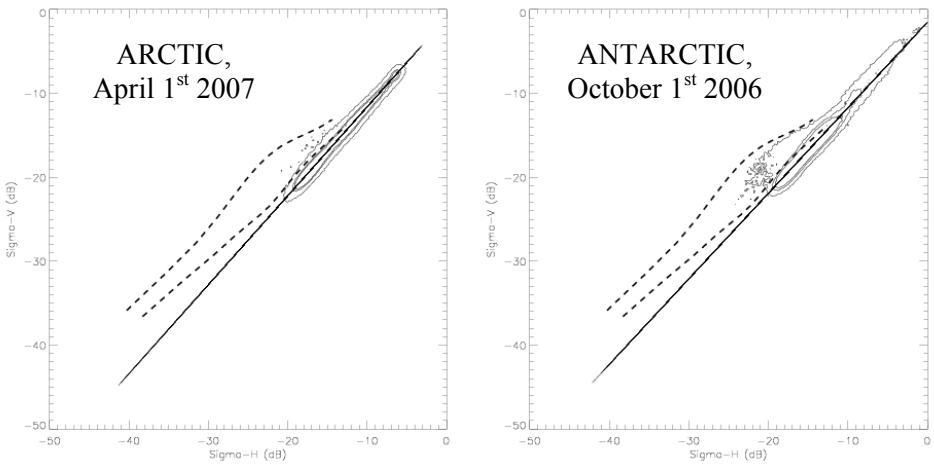

Figure 7 –Histogram (70, 80 and 95%) contours of SeaWinds sea ice backscatter with superimposed *linear ice* and *ocean wind* (NSCAT2, dashed) models

In other words, we observe that the ratio between the horizontally and vertically polarized components of sea ice backscatter (measured at 46 and 54 deg incidence, in dB space) is independent of the backscatter strength and very nearly unit.

How stable is this feature throughout the yearly seasons? In the *northern hemisphere* (see Appendix B1), the levels of sea ice backscatter observed during winter (January through March) are very stable, ranging from -5 to -21 dB for the H-pol component at 46 deg incidence (and -7 to -23 dB for the V-pol component at 54 deg incidence), and adjusting well to a straight ice line model. In the summer, the brightest portion of the sea ice distribution is lost (i.e. the bright multiyear ice signature merges with that of first year ice) and a significant number of data points scatter towards the ocean model (i.e. a number of *mixed ice-water pixels* make appearance). For sea ice that survives the summer melt, the transition to multiyear ice is rather abrupt: the backscatter levels of summer ice (which range from -10 to -20 dB for H-pol at this time of the year) suffer an overall increase of about 5 dB in both the H and V-pol components as the fall season starts (September), after which new data points start filling the dimmest portion of the backscatter distribution (new ice production), bringing it back to its stable winter configuration [Onstott, 1987]. In the *southern hemisphere* (see Appendix B2), most of the sea ice backscatter observed during winter (i.e. July through September) is found between -10 and -20 dB. In contrast to the Arctic case, where bright backscatter usually relates to multiyear ice, the brightest portions of the Antarctic backscatter distribution arise from the ice shelves (Ronne, Ross, Amery, Shackleton, etc…), which also feature larger polarization ratios than multiyear ice. Most of the floating Antarctic ice disappears in the summer, leaving the backscatter from the ice shelves and that from mixed ice-water pixels to dominate the distribution of data points. Note that the presence of mixed pixels is more abundant in the Antarctic than in the Arctic, probably a reflection of the more dynamic environment to which the southern sea ice margin is subject.

A graphical summary of the seasonal dependence of the linear ice model slopes is given in Figure 8 below. The linear model slope is affected by a number of factors, including the presence of ice-water mixed pixels (*MP* in Fig.8 during the austral and boreal summers, negatively biasing the model slope) or backscatter from the ice shelves (late in the austral summer, positively biasing the model slope). To ensure the uniformity of the linear sea ice GMF throughout the yearly seasons, we opt to use the mean winter Arctic and Antarctic slope values in its definition (see Table 1).

Table 1 – Winter sea ice GMF fits: $\sigma^0_{V,ice} = \sigma^0_{H,ice}$*Slope + Offset

	Arctic	Antarctic
Slope	1.06	1.02
Offset	-1.0 dB	-1.5 dB

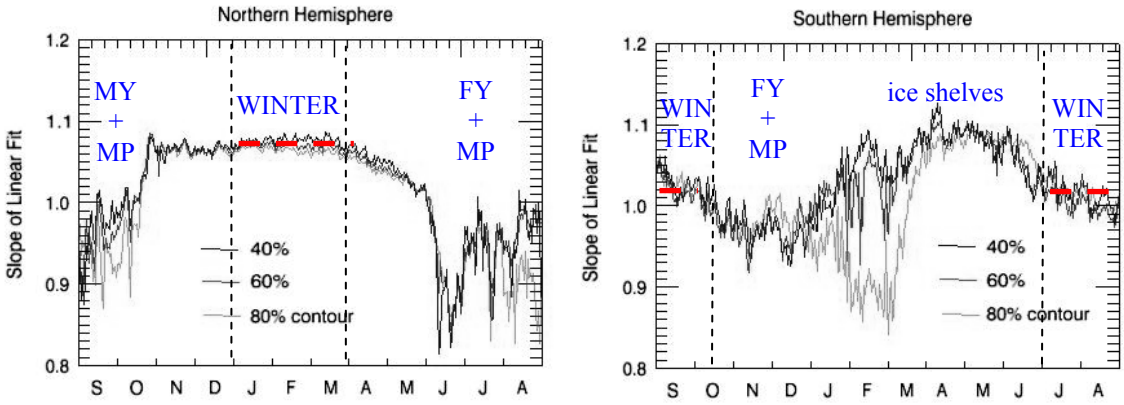

Figure 8 – Daily slopes to linear ice model (Arctic on left and Antarctic on right panel)

b) The distribution of sea ice backscatter about the winter *linear ice model* is Gaussian – see Fig.9.

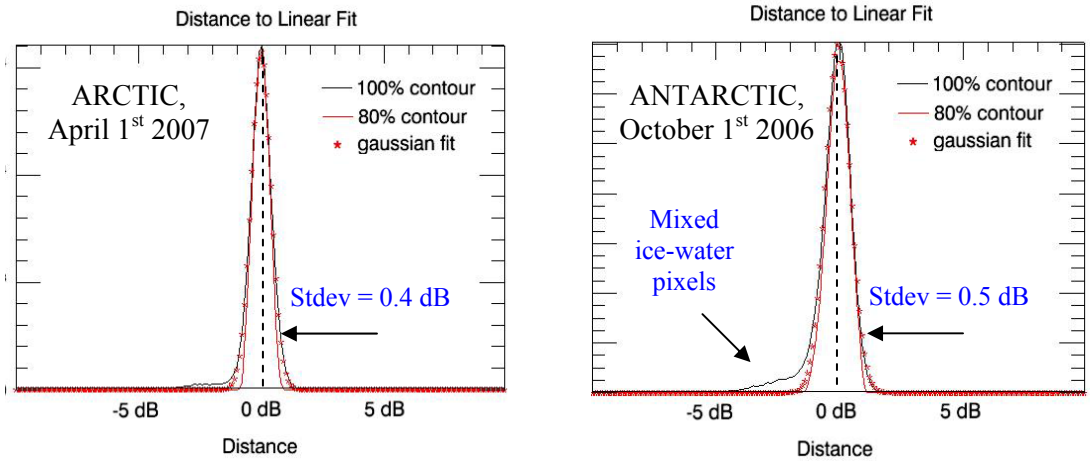

Figure 9 – Histogram of sea ice backscatter distances to linear ice model

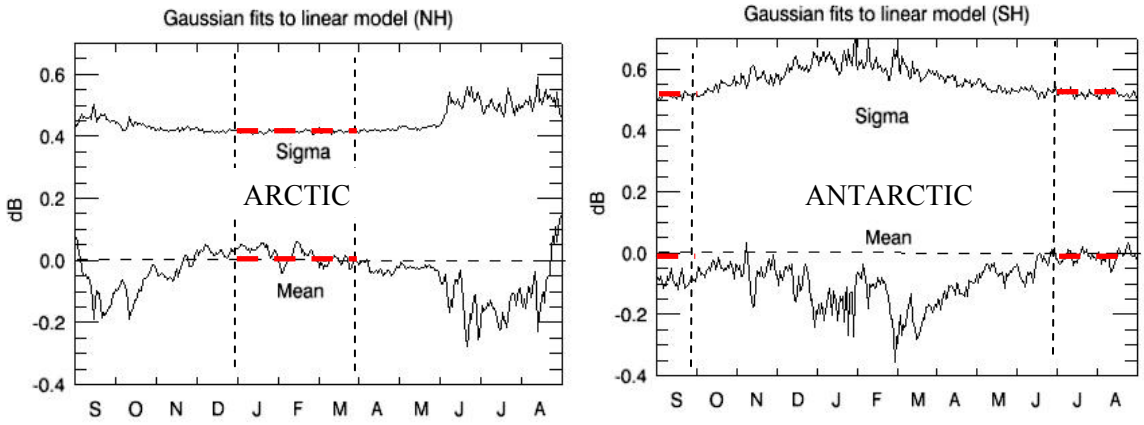

Figure 10 – Gaussian fit parameters (Sigma = Standard deviation; Mean = Bias)

The distribution of sea ice backscatter distances to the linear ice GMF model on the SeaWinds 'fore' and 'aft' measurement subspaces conform to Gaussian functions. A summary of the seasonal dependence of the Gaussian fit parameters (standard deviation and bias) for the

dispersion of data about the winter linear ice model is given in Figure 10 (see also Appendix C). Observe that the increased dispersion of data outside of the selected winter periods relate mainly to the presence of mixed ice-water pixels, which do not adjust to the Gaussian fit.

c) There are no significant traces of azimuthal anisotropy in sea ice backscattered data – see Fig.11.

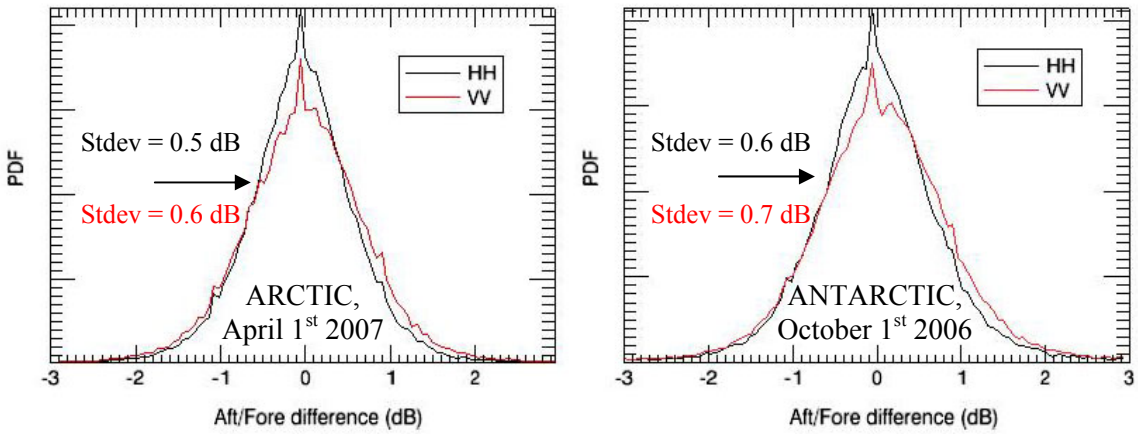

Figure 11 – Azimuthal sea ice backscatter differences

In order to detect azimuthal variability in sea ice backscatter, we calculate the difference between aft and fore backscatter values for H and V-pol components separately – see Figure 11. Since this difference turns out to be commensurate with the natural one-dimensional dispersion of backscatter about the ice model on each measurement subspace (i.e. the variance of the difference equals the sum of the original one-dimensional variances), we conclude that there are no traces of azimuthal anisotropy in sea ice backscatter at Ku-Band. On the other hand, the azimuthal modulation of ocean backscatter (not shown) reaches amplitudes of up to 6-7 dB, indicating that there is a strong ice-ocean discrimination power attached to azimuthal variability.

The lack of correlation between measurements of sea ice backscatter on the fore and aft subspaces means that we can generalize the simple 1-D model of Gaussian dispersion about the linear ice model to the entire measurement space of SeaWinds. Therefore, the probability to find a sea ice backscatter quadruplet a squared distance MLE_{ice} away from the one-dimensional sea ice GMF line is given by a chi-square distribution with three degrees of freedom (see Fig.12) [Johnson, 1994], where:

$$MLE_{ice} = \sum_{i=1,..,N} \frac{(\sigma^0_{obs,i} - \sigma^0_{ice,i})^2}{\mathrm{var}[\sigma^0_{ice}]} \tag{4}$$

$$p(\sigma^0 \mid ice) = \sqrt{\frac{MLE_{ice}}{2\pi}} e^{-MLE_{ice}/2} \tag{5}$$

Always as a function of the dispersion of measurements about the linear ice model, var[σ^0_{ice}]. The expected dispersion for pure ice backscatter points is given in Table 2 below, which excludes the thin cloud of *mixed ice-water pixels* that usually collects on one side of the backscatter distribution (i.e. towards the ocean GMF). The effective discrimination of mixed ice-water pixels may thus call for values of var[σ^0_{ice}] larger than those solely corresponding to pure ice cells.

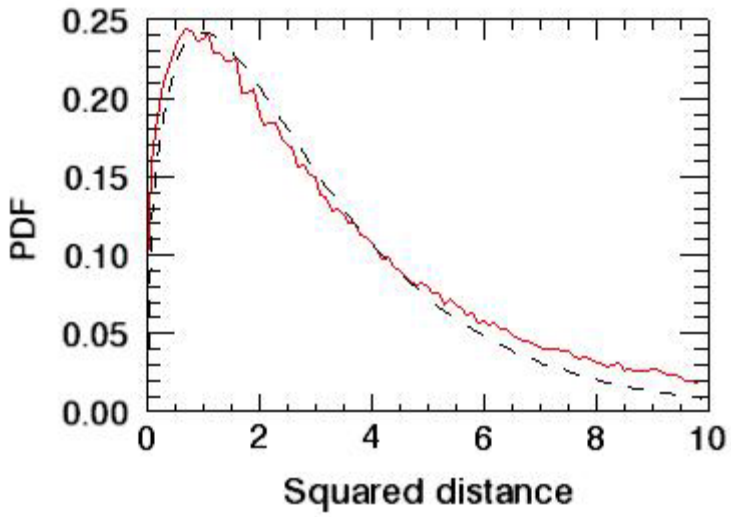

Table 2 – Expected 1-D gaussian scatter about linear sea ice GMF

	Arctic	Antarctic
Std Dev	0.4 dB	0.5 dB

Figure 12 – Probability distribution of sea ice backscatter about the sea ice GMF: red is the observed distribution normalized to unit area, and dashed is modeled from Eq (5).

At this point, we have obtained a linear GMF for winter sea ice backscatter in the space of SeaWinds measurements, and we have characterized the variance of SeaWinds data around this model, providing a formal expression for the conditional probability $p(\sigma^0|ice)$. Still, there are a number of question pertaining the presence and detection of mixed ice-water pixels, namely: what is the proper definition of ice edge when low sea ice concentrations are present? Can we adjust the definition of sea ice edge by modifying the expected variance about the ice linear GMF? Do the resulting sea ice probabilities relate to sea ice concentrations?

5 Algorithm implementation and validation

As already introduced, the implementation of the KNMI sea ice detection algorithm using SeaWinds data requires the calculation of the posterior ice probability as:

$$p(ice \mid \sigma^0) = \frac{p(\sigma^0 \mid ice)\, p_0(ice)}{p(\sigma^0 \mid ice)\, p_0(ice) + p(\sigma^0 \mid wind)\, p_0(wind)} \tag{1}$$

where

$$p(\sigma^0 \mid ice) = \sqrt{\frac{MLE_{ice}}{2\pi}}\, e^{-MLE_{ice}/2} \qquad p(\sigma^0 \mid wind) = \frac{1}{L}\, e^{-MLE_{wind}/L} \tag{3) \& (5)}$$

and

$$MLE_{wind} = \frac{1}{\langle MLE \rangle} \sum_{i=1,\ldots,N} \frac{(\sigma^0_{obs,i} - \sigma^0_{wind,i})^2}{\mathrm{var}[\sigma^0_{wind,i}]} \qquad MLE_{ice} = \sum_{i=1,\ldots,N} \frac{(\sigma^0_{obs,i} - \sigma^0_{ice,i})^2}{\mathrm{var}[\sigma^0_{ice}]} \tag{2) \& (4)}$$

in terms of the normalized squared distances to the Ku-Band ocean wind and ice GMFs. The local prior probabilities for ice and wind are initially set to $p_0(ice) = p_0(wind) = 0.50$ (reflecting low initial certainty), and then become updated daily using relaxed versions of the previous day posteriors as:

$$p_0(ice) = \begin{cases} 0.50 & if\ p(ice \mid \sigma^0) > 0.30 \\ 0.15 & if\ p(ice \mid \sigma^0) < 0.30 \end{cases} \tag{6}$$

These settings have been chosen after a preliminary trial-and-error study to maximize the level of historic information passed on to the discrimination algorithm, without contradicting the update information carried by new measurements. These processing steps are illustrated in Figure 13 below. In panel A, the distance of backscatter to the ice model is seen to provide a strong ice-water contrast, only disturbed by local structures on the ocean (e.g. see the Bering Sea in Panel A below) that arise from σ^0-quadruplets lying close to the ice model. In panel B, the distance of backscatter to the ocean wind model also provides a good ice-water contrast, only weakened at extreme high latitudes by the combined effects of a reduced azimuthal diversity in SeaWinds measurements and the presence of bright multiyear ice (which lies close to the high windspeed portion of the ocean model). In panel C, the *a priori* ice probability is built from the sea ice probability map computed for the previous day. The graininess in the raw $p(\sigma^0|class)$ maps is caused by the SeaWinds daily sampling density in the selected projection grid (i.e. SSM/I polar stereographic, with 12.5 km pixels at 70 deg. latitude).

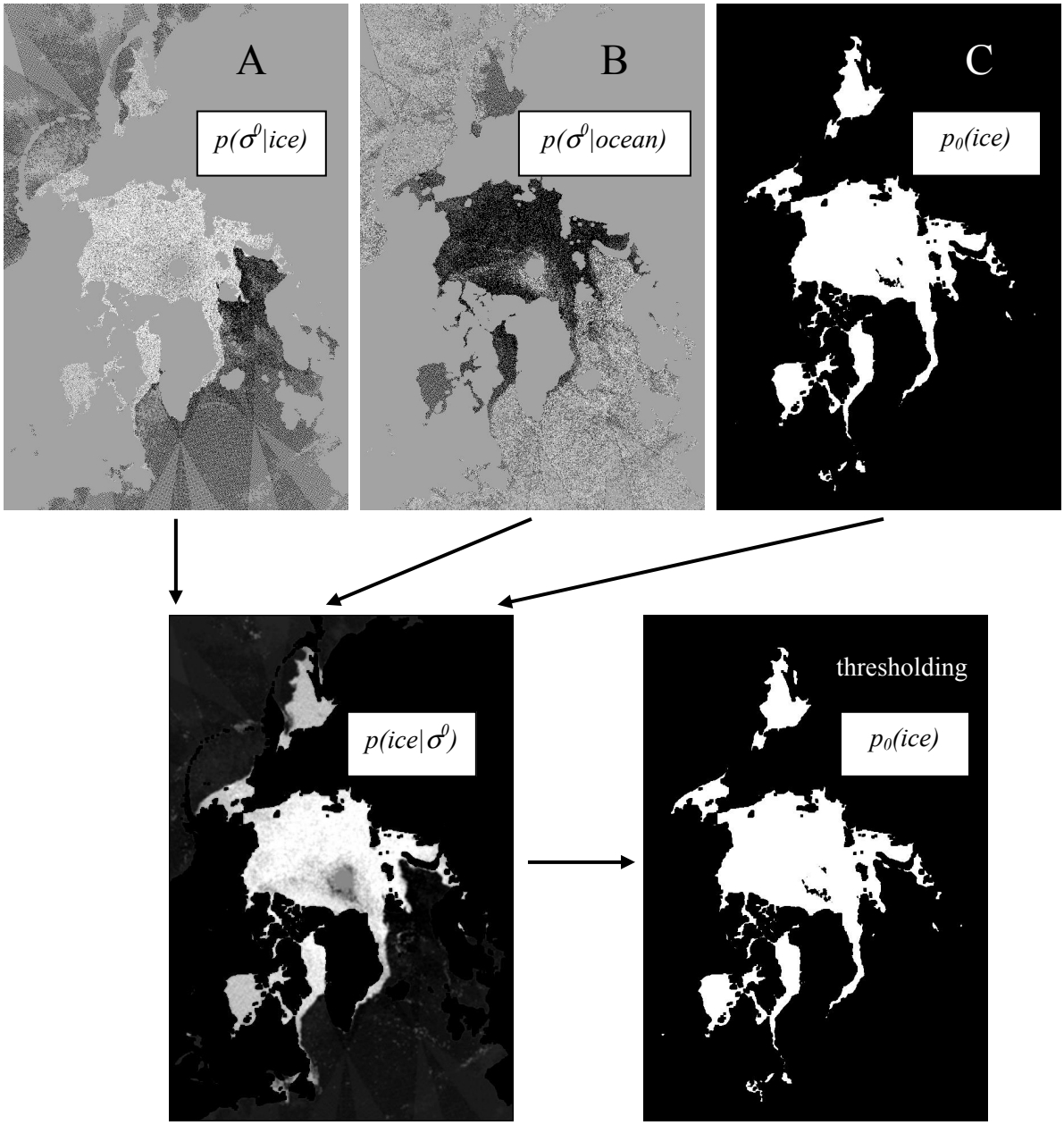

Figure 13 – Bayesian probability combination and thresholding

Finally, the SeaWinds KNMI sea ice discrimination algorithm utilizes a probability threshold of 0.45 in the generation of its sea ice masks.

Validation

As validation source, we use daily gridded AMSR-E sea ice concentrations from Aqua (AE SI12 v.001 from EOS data gateway, [Cavalieri, 2004]). This 12.5 km sea ice concentration product is generated using the Enhanced NASA Team (NT2) algorithm, which has proven accurate to within 10-15% error against

clear sky visible sea ice concentrations ([Meier, 2005], [Cavalieri, 2006]). The accuracy of the AMSR (NT2) sea ice concentration algorithm is worst in the summer months, when it is most affected by weather effects, unresolved thin or low concentration ice types, and surface melt effects [Markus, 2000]. However, the wintertime AMSR (NT2) sea ice extents (with a 15% ice concentration edge) prove to lie within 10 km of the ice edge extracted from RADARSAT SAR and MODIS image composites [Heinrichs, 2006]. An additional source of validating data are the US National Ice Center (NIC) sea ice charts, which are produced from combined satellite records that include visible, infrared and microwave imagery [Dedrick, 2001]. Caution must be exercised when using NIC charts as a validation source, since they tend to rely heavily on QUIKSCAT and SSM/I imagery.

As a preliminary validation exercise, we compare the daily AMSR NT2 sea ice extent estimates and the SeaWinds (QSCAT) Real Time BYU sea ice masks during the period spanning from September 15th 2006 through September 15th 2007 (see Fig.14). The extent calculations are performed on polar 12.5x12.5 km^2 stereographic projection grids (true latitude at 70 deg), using a common polar-stereo 12.5 km landmask (GSFC II) with a 25 km coastal filter.

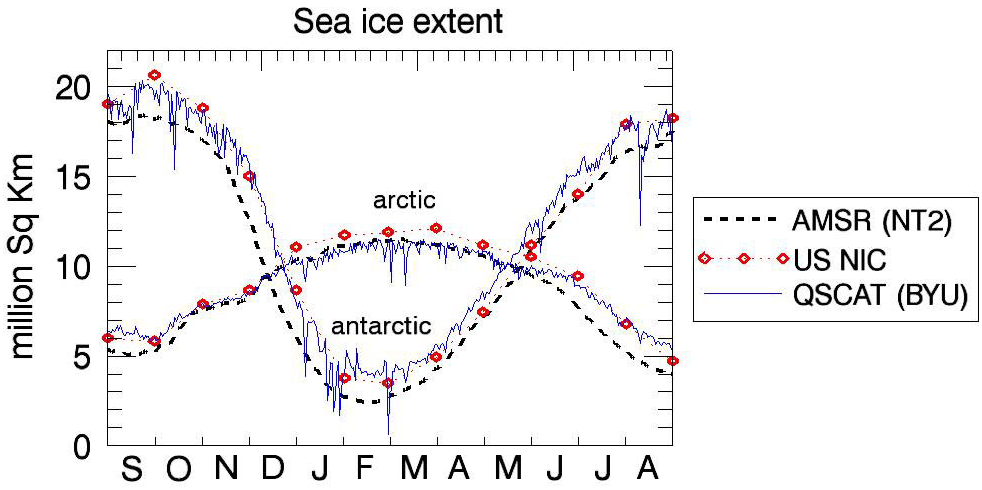

Figure 14 – Daily sea ice extent estimates from AMSR NT2 and SeaWinds BYU algorithms

This figure shows that the SeaWinds BYU sea ice mask included in the NOAA/NESDIS Real Time BUFR Geophysical Data Product is rather conservative relative to the passive microwave algorithm (except in the arctic winter), and that user complaints about erratic winds over sea ice may be associated with occasional glitches in the BYU masks, which also contain a significant amount of noise along the ice edge [Meier, 2008] (see also Appendix D). We observe, as it has been noted in [Meier, 2006], that the smallest difference between the NIC and AMSR (NT2) extents occurs during the freeze-up period, when the existing ice refreezes but before substantial new ice has formed, and that the AMSR (NT2) algorithm tends to underestimate the sea ice extent relative to the NIC masks at all other seasons (i.e. see also [Markus, 2002]).

Next, the daily sea ice extents are calculated using the SeaWinds KNMI algorithm for various levels of expected ice model variance, var[σ^0_{ice}], and compared against our previous reference AMSR (NT2) and NIC sea ice masks (see Fig.15).

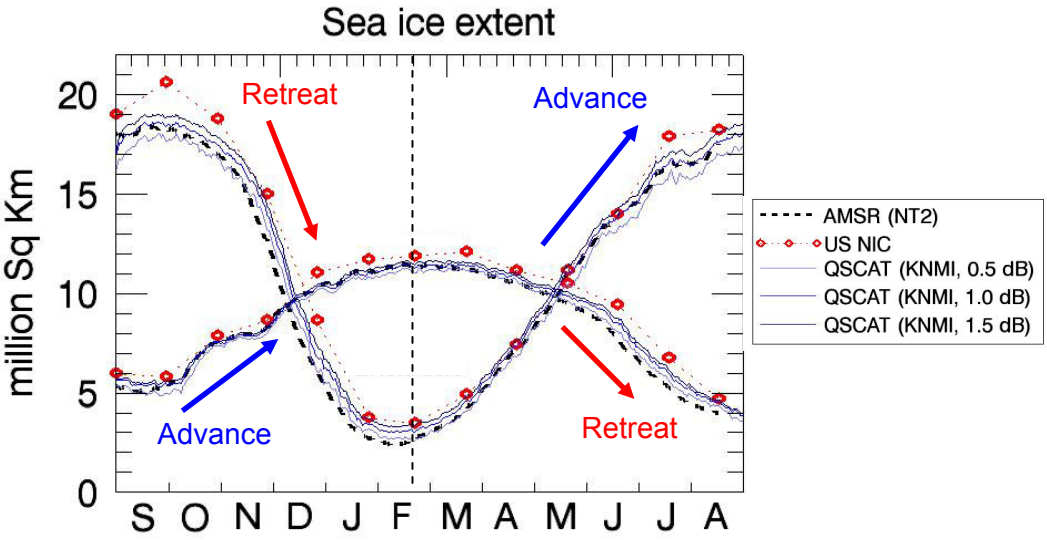

Figure 15 – Performance of SeaWinds KNMI algorithm (ice model variance = 0.5, 1.0 and 1.5 dB): advance (freeze-up) and retreat (melt) cycles

First note that the sea ice extent produced by the SeaWinds KNMI algorithm increases with the ice model variance, reflecting the fact that more mixed ice-water pixels become absorbed by the ice model as its allowance for distant backscatter points increases (from 0.5 to 1.5 dB). The sensitivity of the KNMI algorithm to the expected ice model variance is greatest in regions with low ice concentration (i.e. the marginal ice zones, especially during the austral and boreal summers), and lowest during freeze-up in both hemispheres (see Fig.16 below).

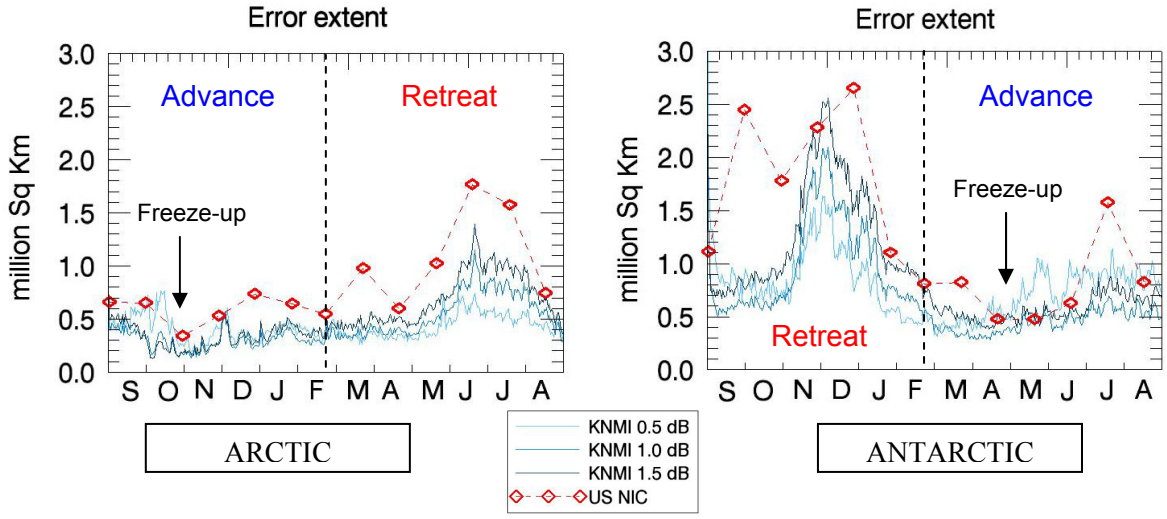

Figure 16 – Total extent error between SeaWinds KNMI, NIC and AMSR (NT2) sea ice masks

It is precisely during freeze-up that the best agreement is observed between the SeaWinds KNMI algorithm (more or less regardless of the ice model variance) and the AMSR (NT2) and NIC sea ice extent estimates. While there is good agreement between the AMSR(NT2) and SeaWinds KNMI ice masks during the ice advance (fall and winter) months (with a total extent error below 5%), the total extent error reaches 10-15% during sea ice retreat (spring and summer), where AMSR appears negatively biased relative to SeaWinds (with SeaWinds still short of the NIC edge). The KNMI ice model variance that provides the best extended winter match to the AMSR (NT2) algorithm is 1.0 dB (c.f. Table 2, see Fig.17 below), although an improved agreement with the NIC charts could call for even larger values.

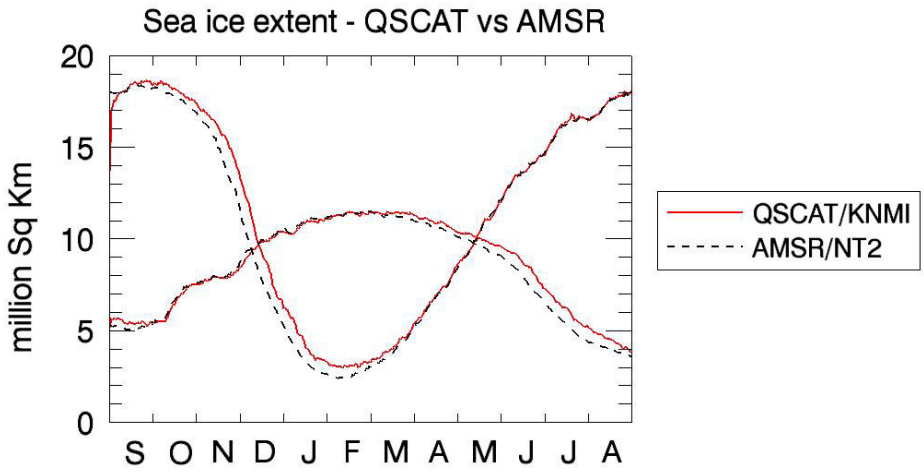

Figure 17 - Daily sea ice extent from AMSR (NT2) and SeaWinds KNMI (1.0 dB) algorithms

The ultimate selection of the SeaWinds KNMI ice variance parameter should be determined by an independent validation effort using e.g. a visible sensor during the summer months. In order to illustrate the strengths and weaknesses of the new SeaWinds KNMI algorithm, we study and comment on a few particular cases, occurring every 15th day of the month and starting September 2006 (see Fig.18 through Fig.30 below). To note:

i) *Blind spot*: The polar region observed by neither AMSR nor SeaWinds due to satellite inclination and observation geometry is masked out and assumed to be ice covered. The blind spot extends for 1 degree about the poles for AMSR, and 2 degrees for SeaWinds. In practice, the SeaWinds KNMI blind spot radius is extended to 5 degrees because of poor algorithm performance at extreme high latitudes (due to the combined effects of bright multiyear backscatter and poor azimuthal diversity).

ii) *New ice production*: The production of new ice may pass undetected to the scatterometer (see the Laptev and Kara Seas in October, Fig.19; Hudson Bay in November, Fig.20; and the Okhotsk and Bering Seas in December, Fig.21 below). It is not that new ice (1-2 days old) is missing in the SeaWinds KNMI probability maps, but it lies below the selected detection threshold. Increasing the ice model variance and/or lowering the detection threshold will improve the chances of its detection, but at the cost of increasing the background noise (i.e. the number of ocean wind cells misclassified as ice). Difficulties for SeaWinds in detecting new ice less than 15 cm in thickness at the sea ice edge have been already reported in [Abreu, 2002]. On the other hand, the AMSR (NT2) algorithm proves very sensitive to the production of new ice.

iii) *Melt onset*: The SeaWinds sea ice discrimination algorithm is more resistant to melt effects than AMSR's (NT2). Even if there is a significant amount of melt water drenching the upper layers of sea ice (thus obscuring its radiometric signature), the backscatter signature still differs from that of the ocean wind and a high probability of ice is eventually assigned.

iv) *Evolution of the sea ice backscatter signature*: The strength of backscatter, and in particular the presence of bright (multiyear and shelf) ice structures, makes it possible to retrace the production and evolution (drift) of sea ice in the northern and southern hemispheres.

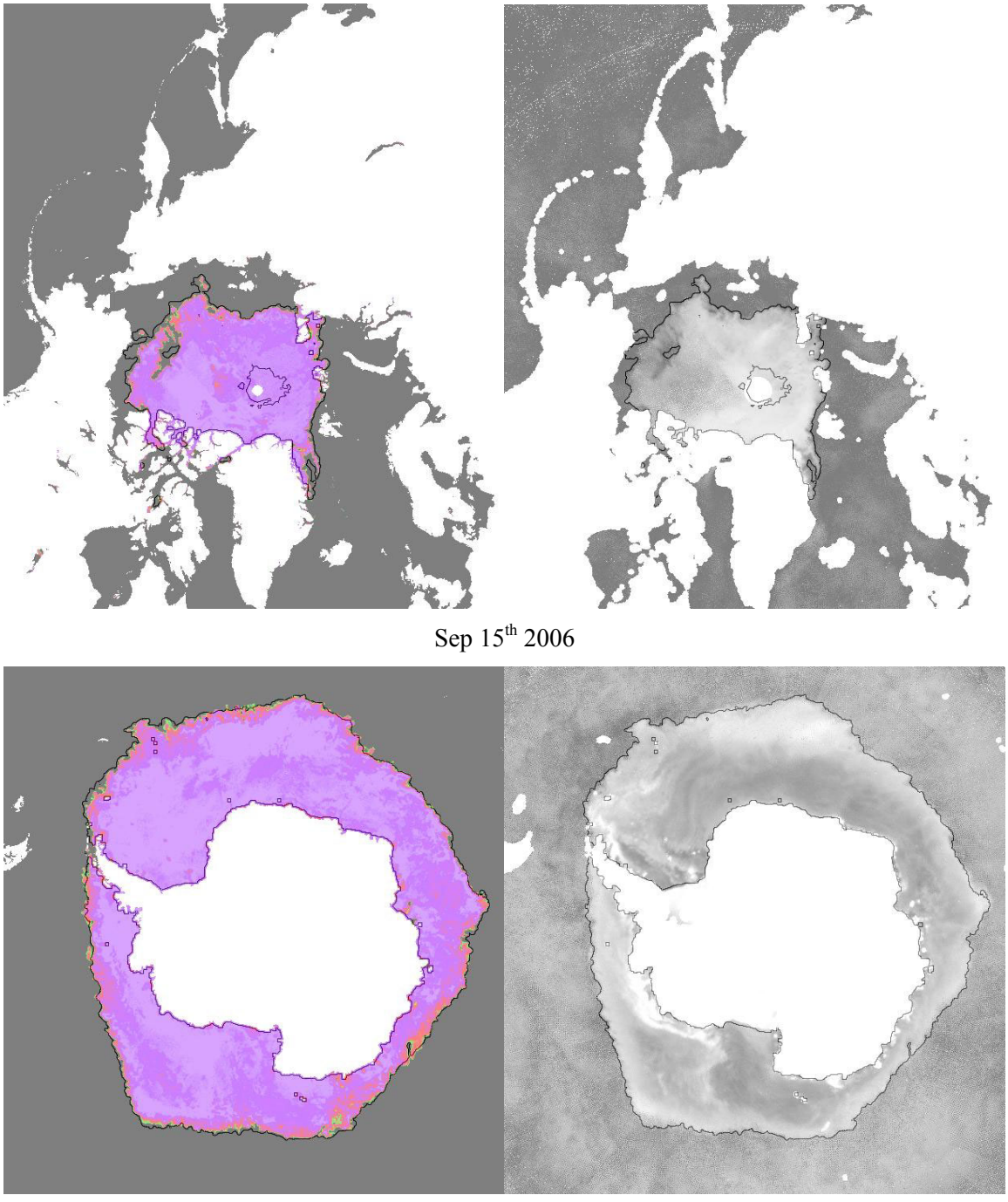

Sep 15th 2006

Figure 18 – QSCAT KNMI (1.0 dB) ice edge vs AMSR sea ice concentration (LEFT) and on QSCAT V-pol backscatter background (RIGHT)

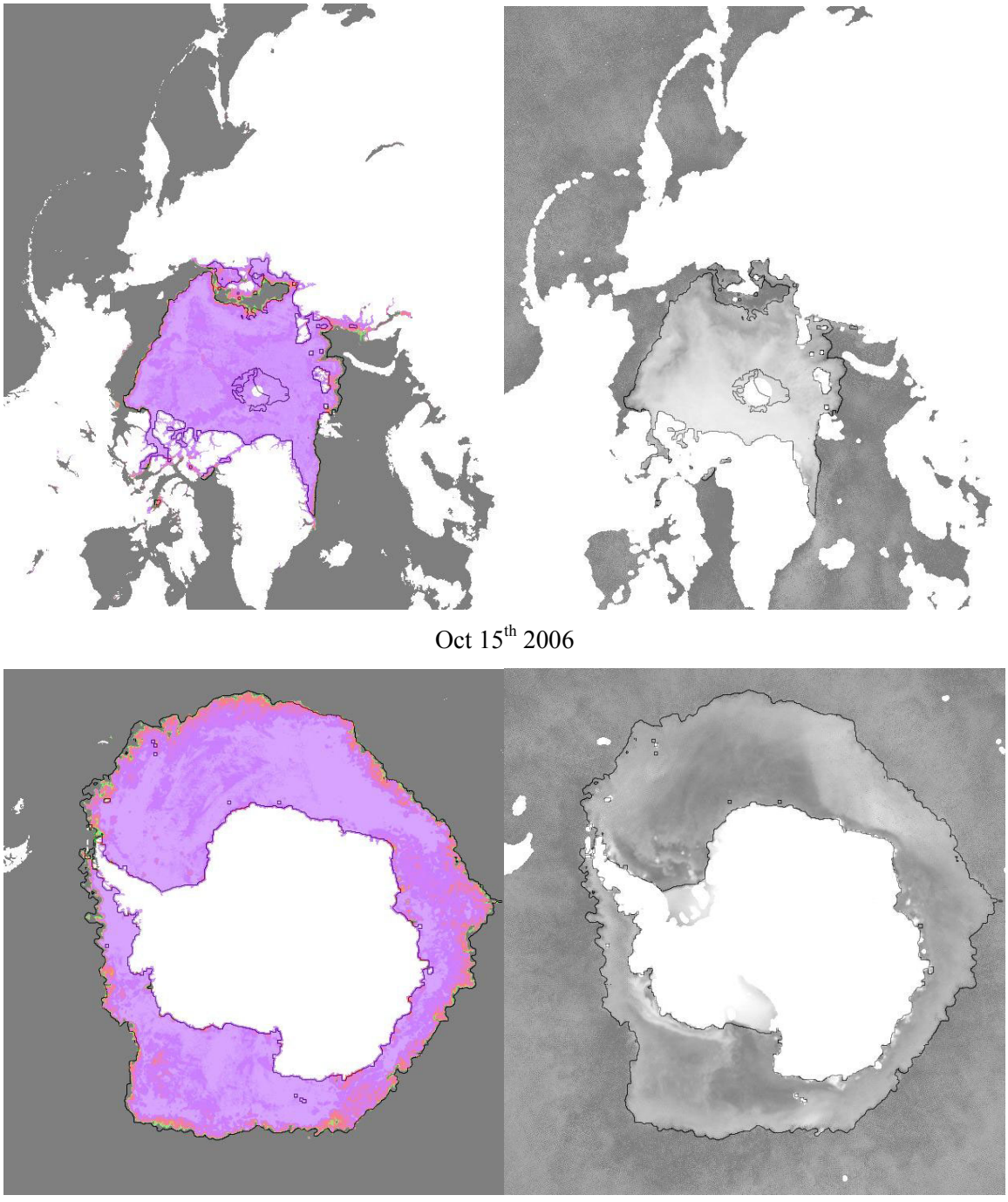

Oct 15th 2006

Figure 19 – QSCAT KNMI (1.0 dB) ice edge vs AMSR sea ice concentration (LEFT) and on QSCAT V-pol backscatter background (RIGHT)

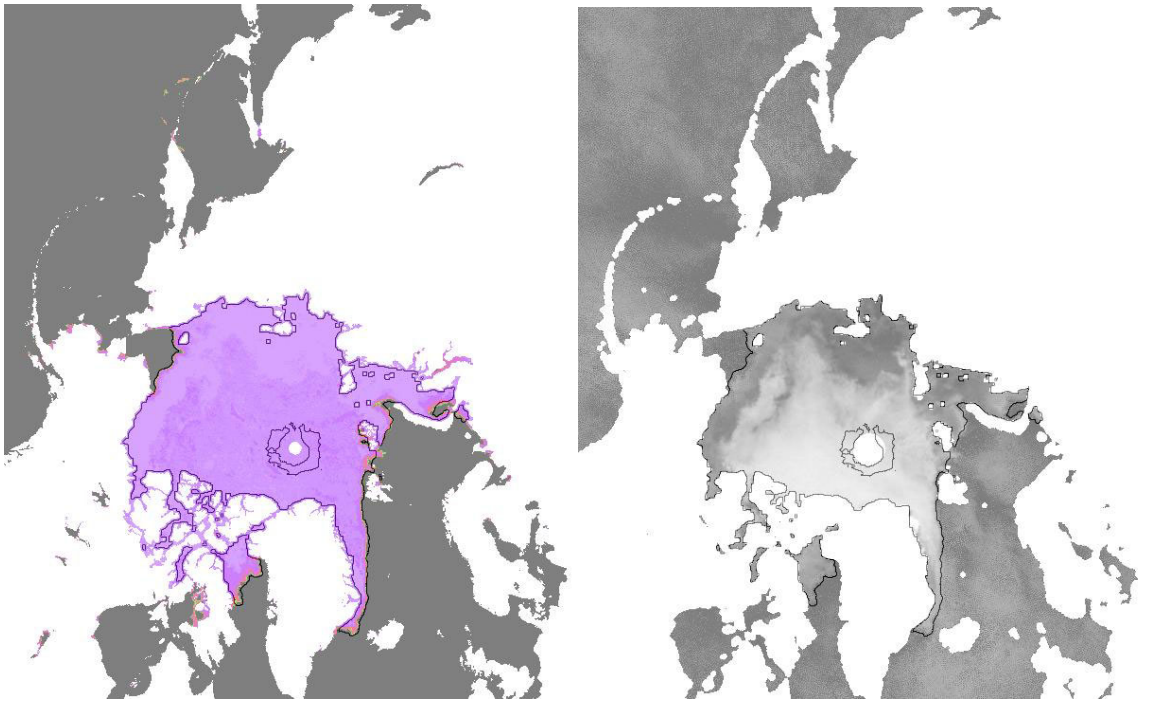

Nov 15th 2006

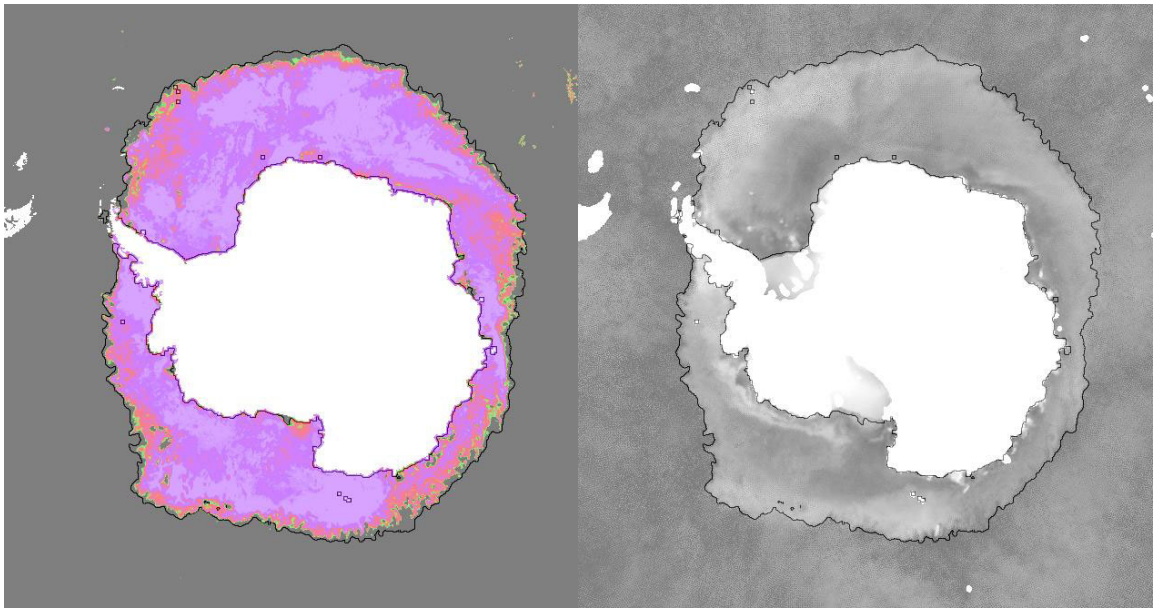

Figure 20 – QSCAT KNMI (1.0 dB) ice edge vs AMSR sea ice concentration (LEFT) and on QSCAT V-pol backscatter background (RIGHT)

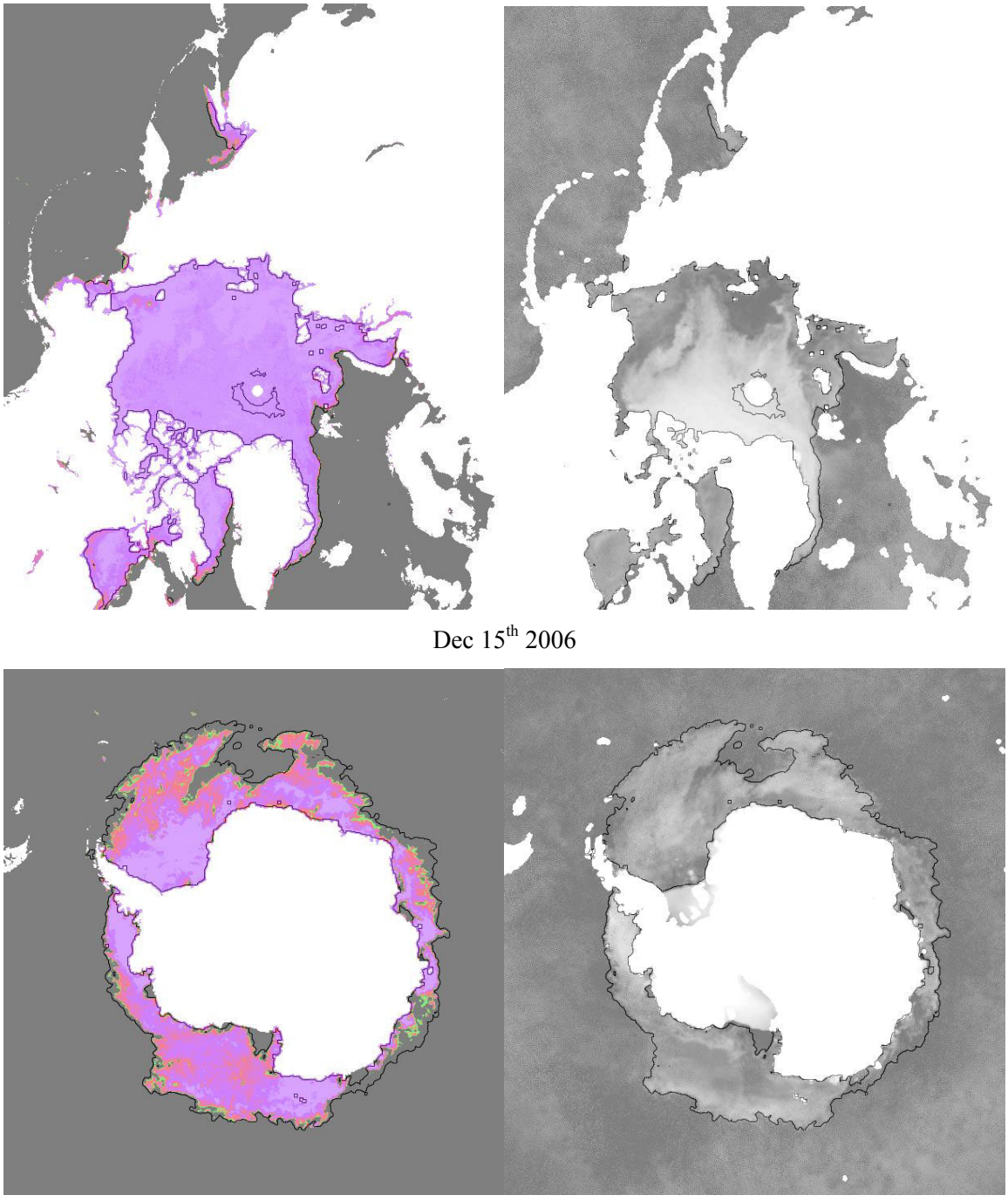

Dec 15th 2006

Figure 21 – QSCAT KNMI (1.0 dB) ice edge vs AMSR sea ice concentration (LEFT) and on QSCAT V-pol backscatter background (RIGHT)

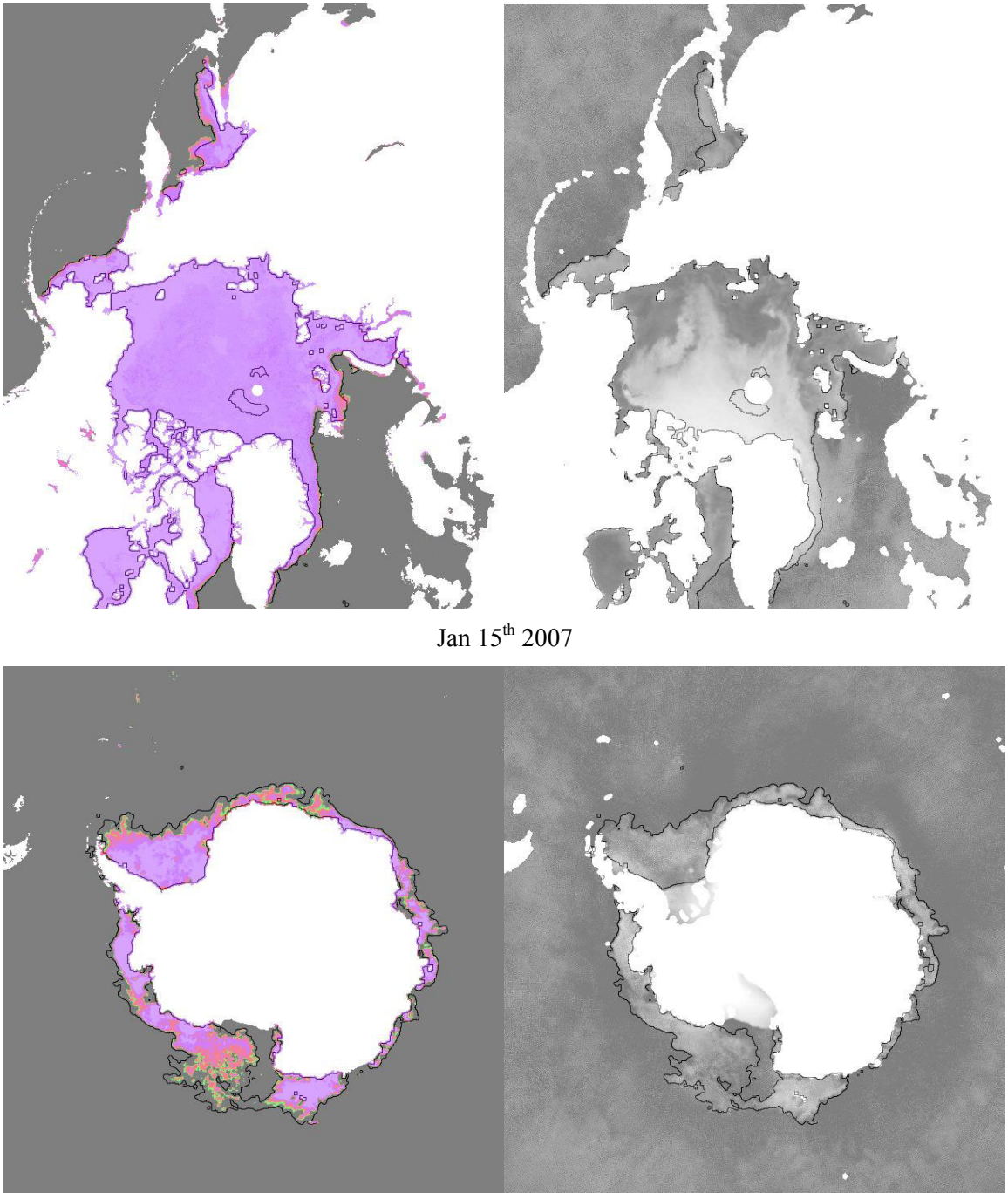

Jan 15th 2007

Figure 22 – QSCAT KNMI (1.0 dB) ice edge vs AMSR sea ice concentration (LEFT) and on QSCAT V-pol backscatter background (RIGHT)

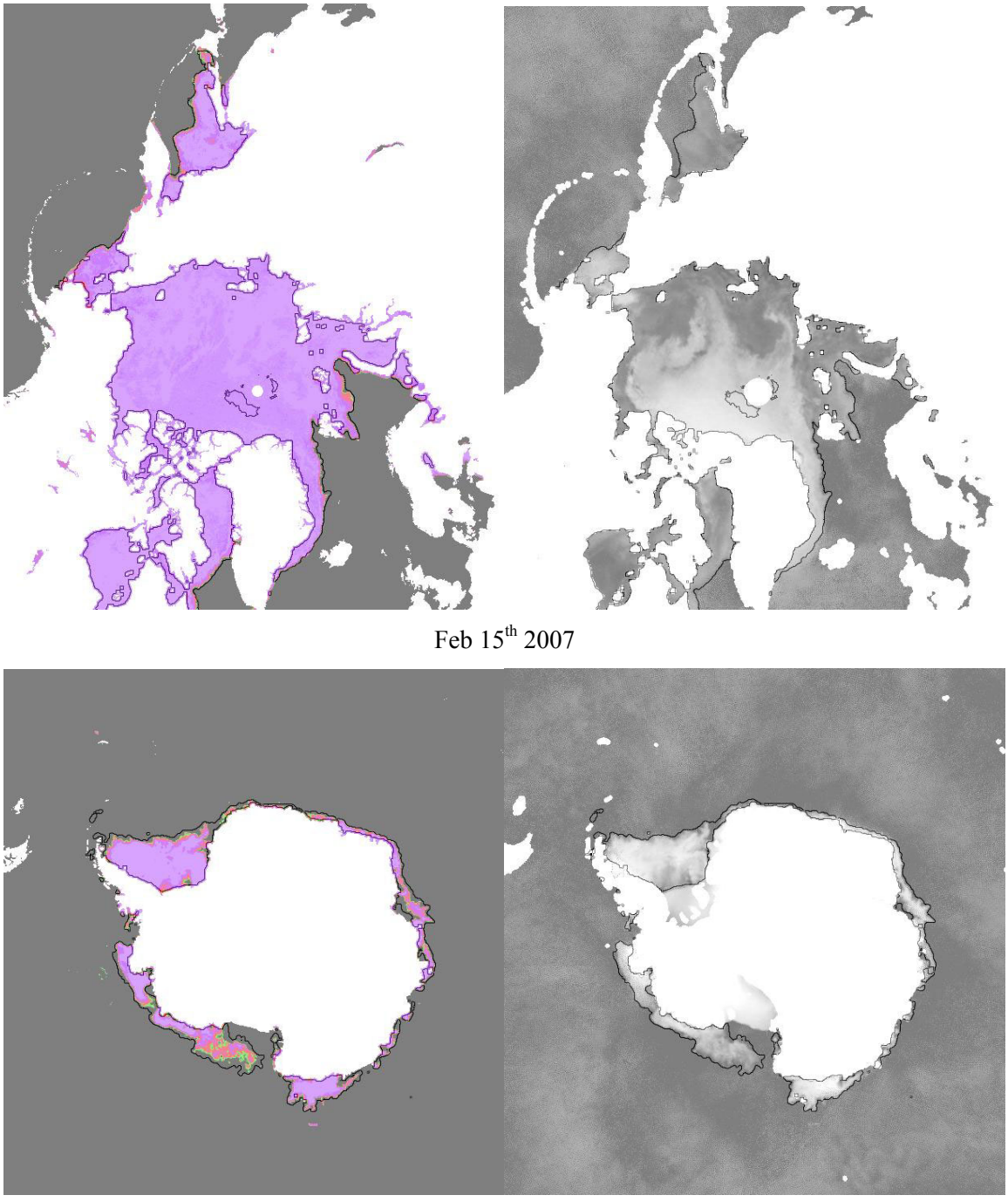

Feb 15th 2007

Figure 23 – QSCAT KNMI (1.0 dB) ice edge vs AMSR sea ice concentration (LEFT) and on QSCAT V-pol backscatter background (RIGHT)

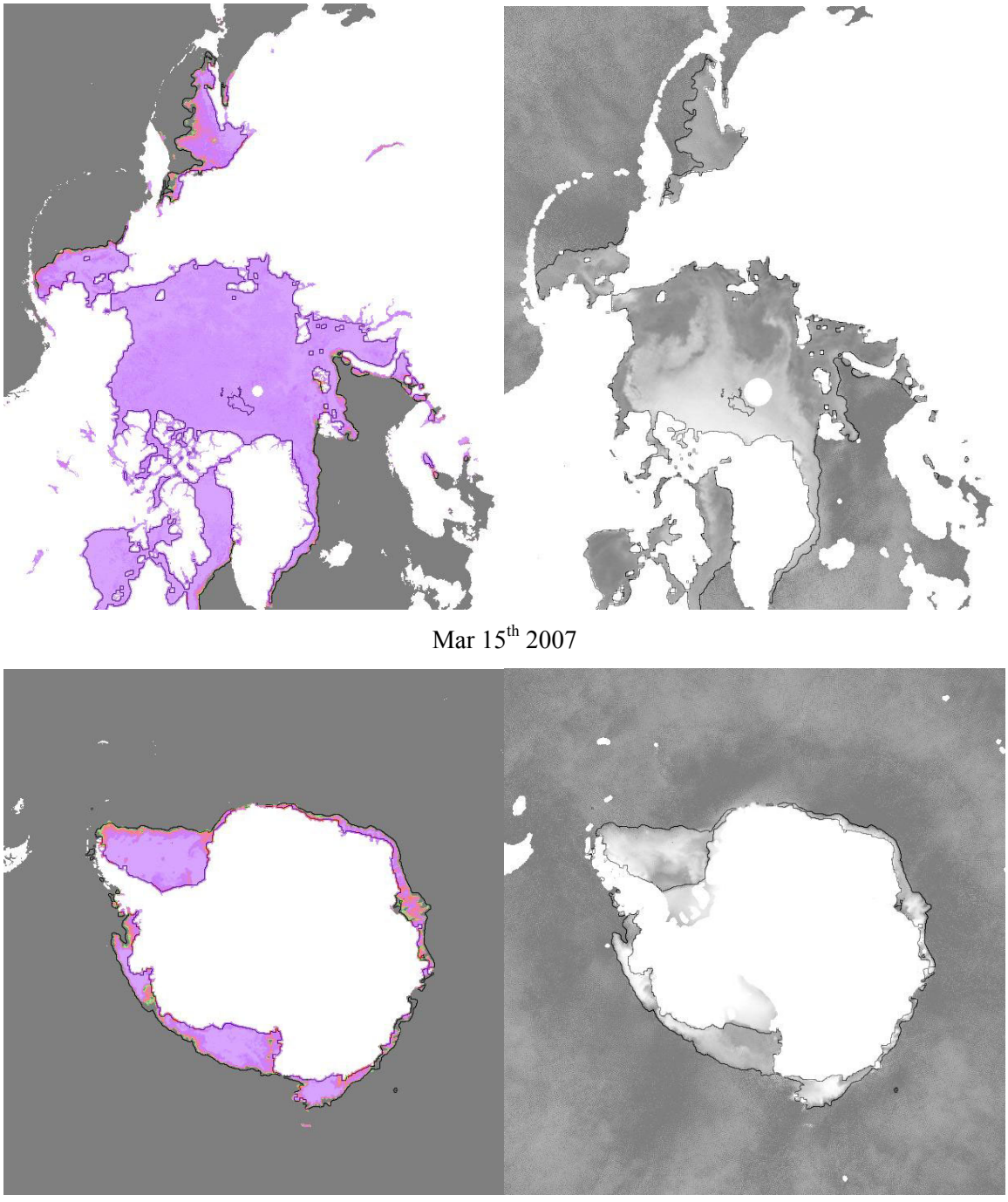

Mar 15th 2007

Figure 24 – QSCAT KNMI (1.0 dB) ice edge vs AMSR sea ice concentration (LEFT) and on QSCAT V-pol backscatter background (RIGHT)

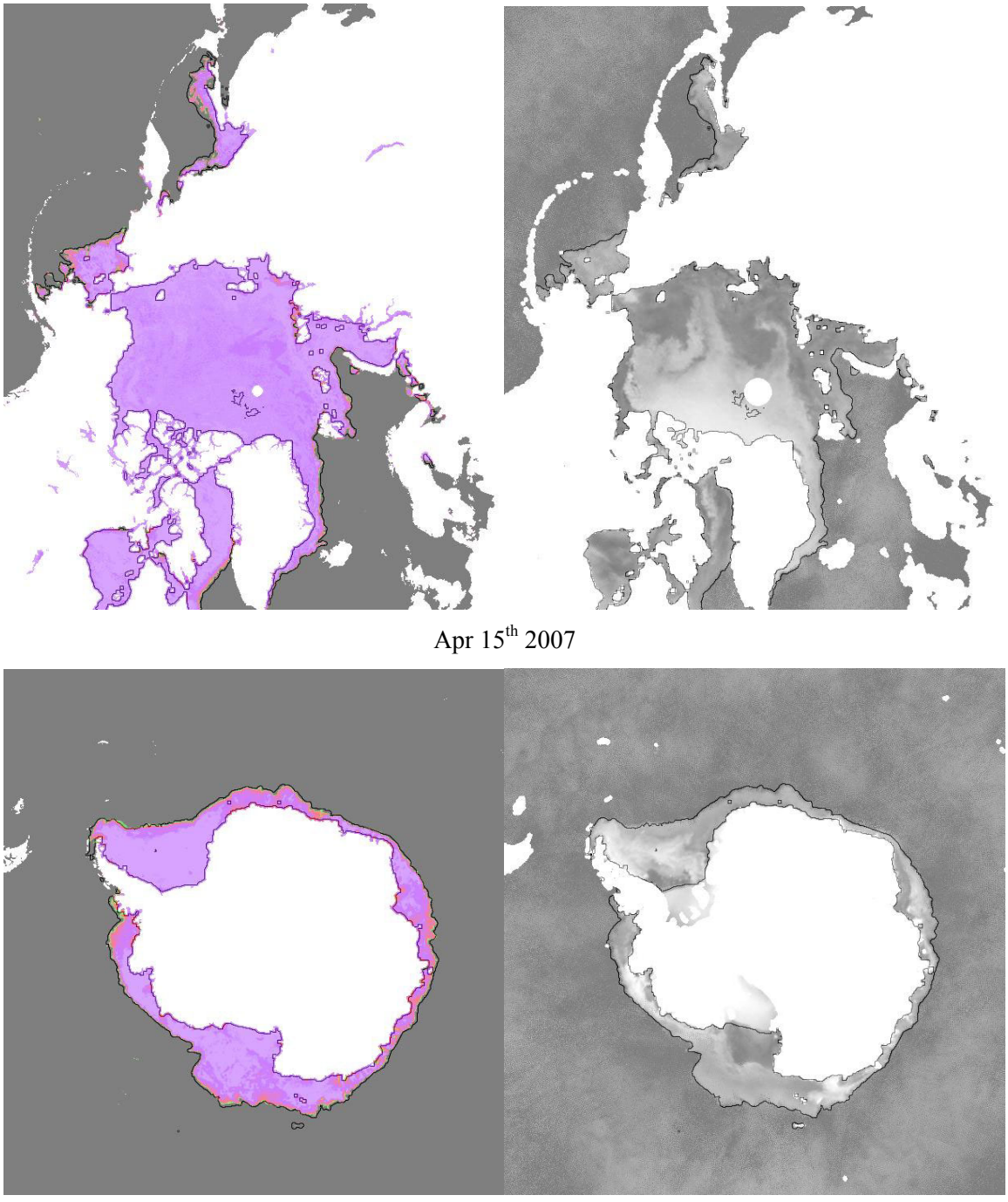

Apr 15th 2007

Figure 25 – QSCAT KNMI (1.0 dB) ice edge vs AMSR sea ice concentration (LEFT) and on QSCAT V-pol backscatter background (RIGHT)

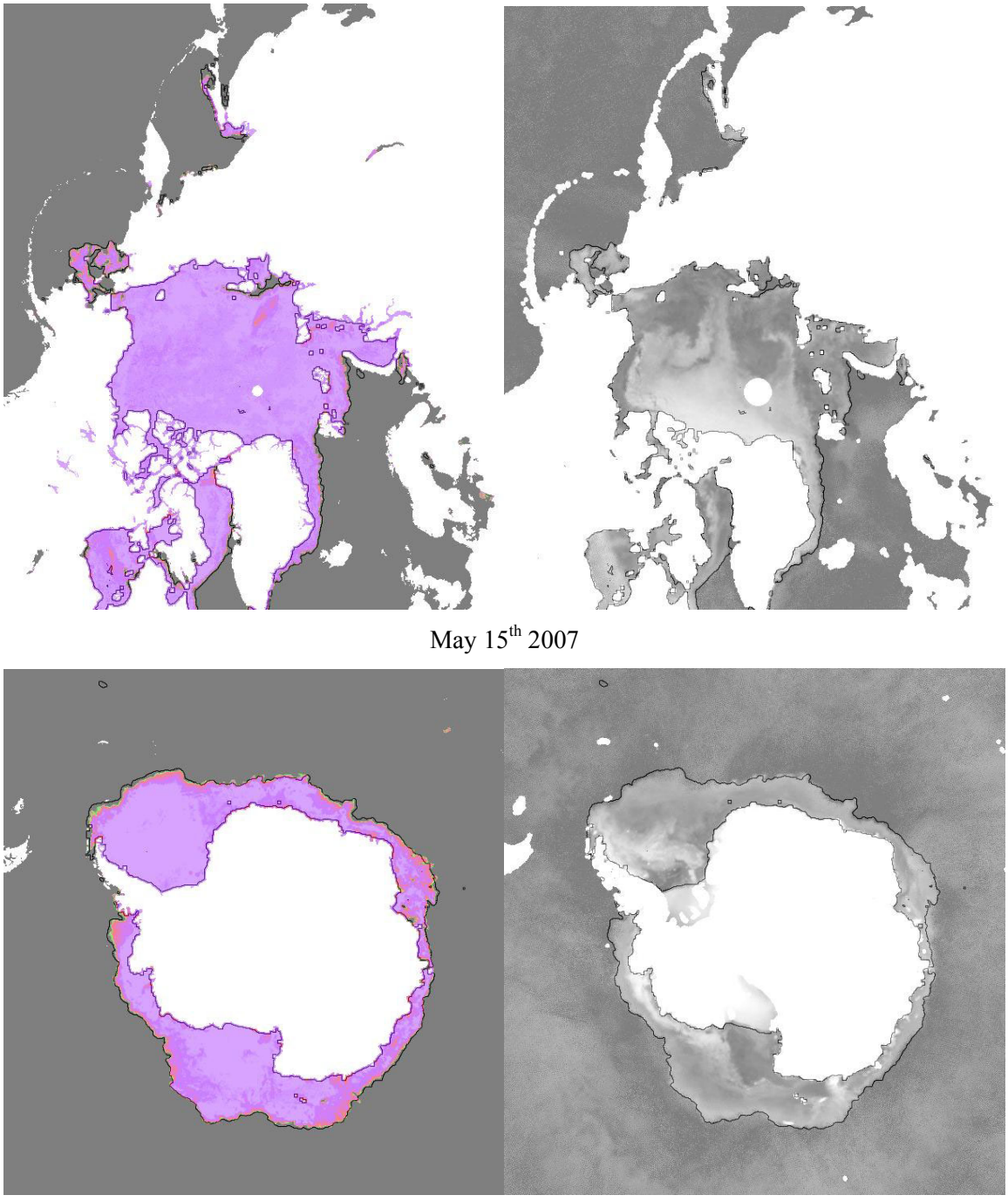

May 15th 2007

Figure 26 – QSCAT KNMI (1.0 dB) ice edge vs AMSR sea ice concentration (LEFT) and on QSCAT V-pol backscatter background (RIGHT)

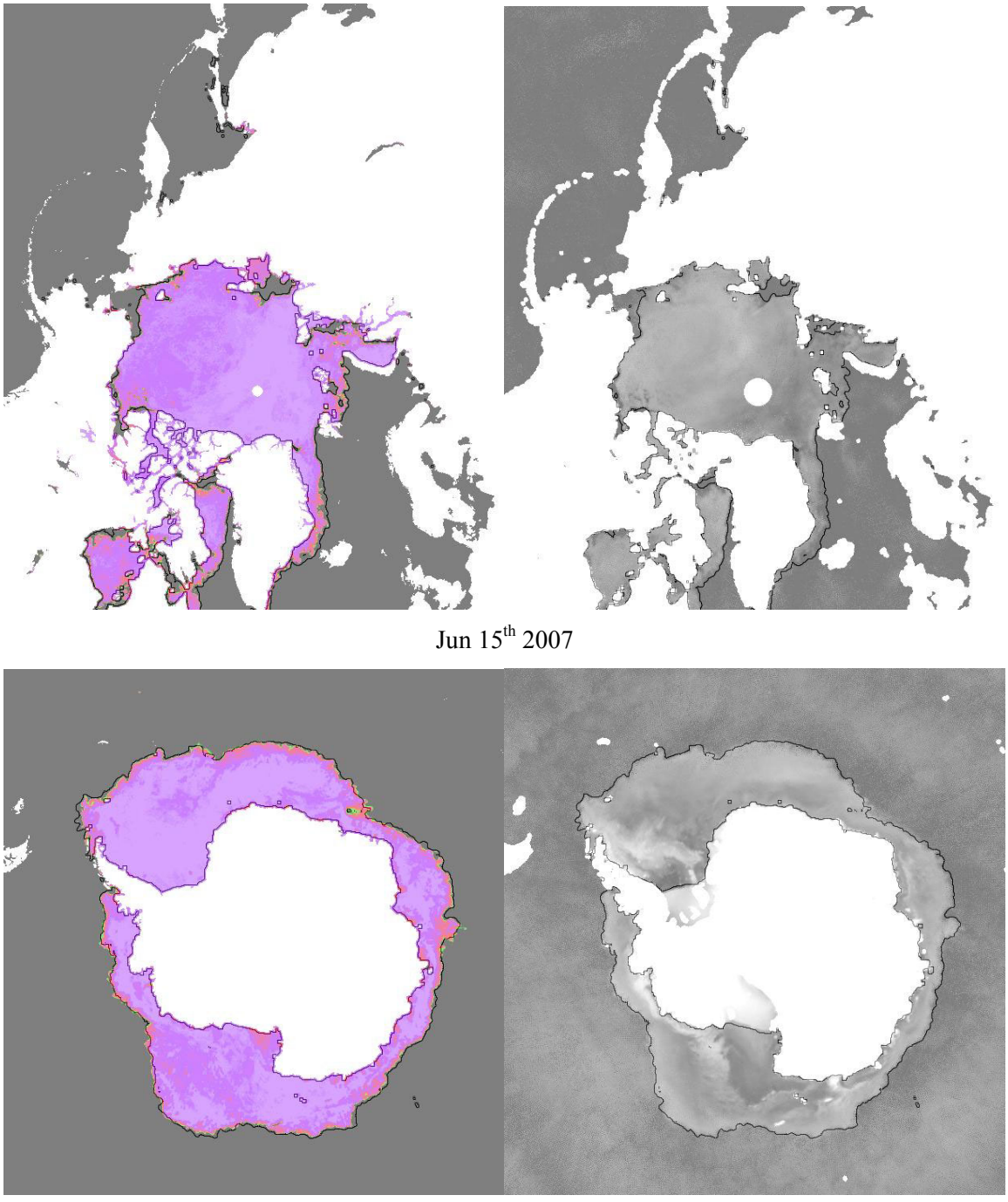

Jun 15th 2007

Figure 27 – QSCAT KNMI (1.0 dB) ice edge vs AMSR sea ice concentration (LEFT) and on QSCAT V-pol backscatter background (RIGHT)

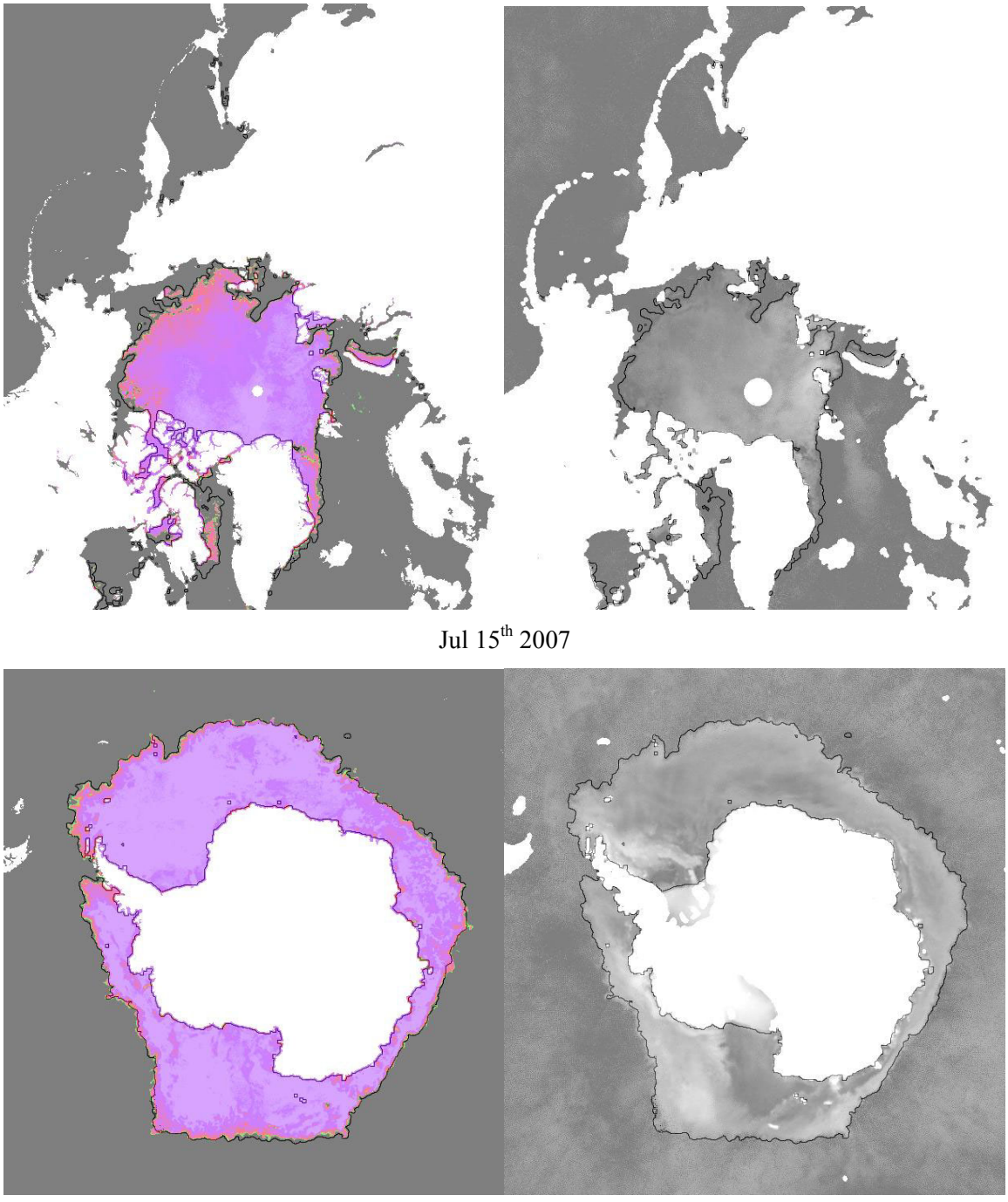

Jul 15th 2007

Figure 28 – QSCAT KNMI (1.0 dB) ice edge vs AMSR sea ice concentration (LEFT) and on QSCAT V-pol backscatter background (RIGHT)

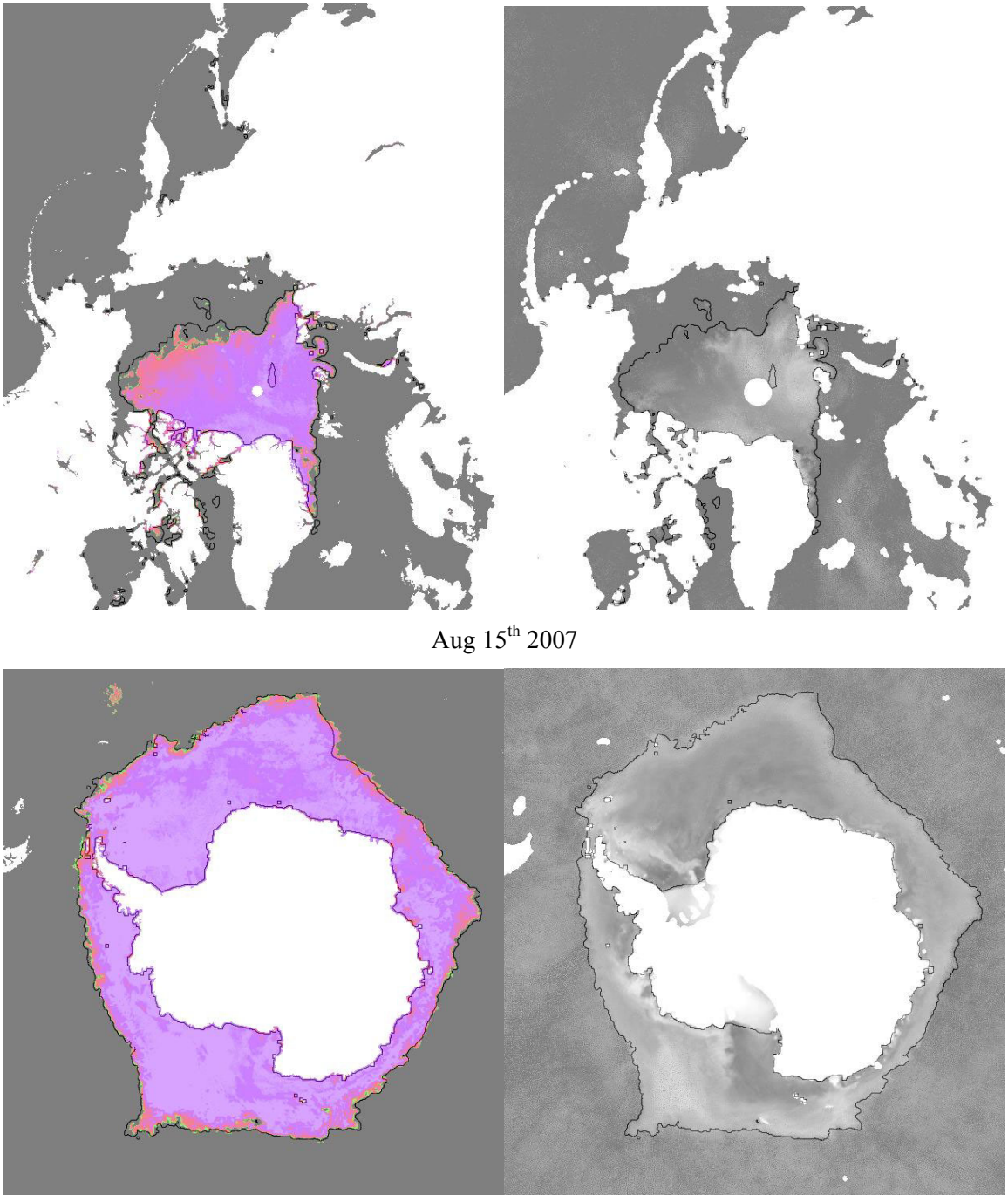

Aug 15th 2007

Figure 29 – QSCAT KNMI (1.0 dB) ice edge vs AMSR sea ice concentration (LEFT) and on QSCAT V-pol backscatter background (RIGHT)

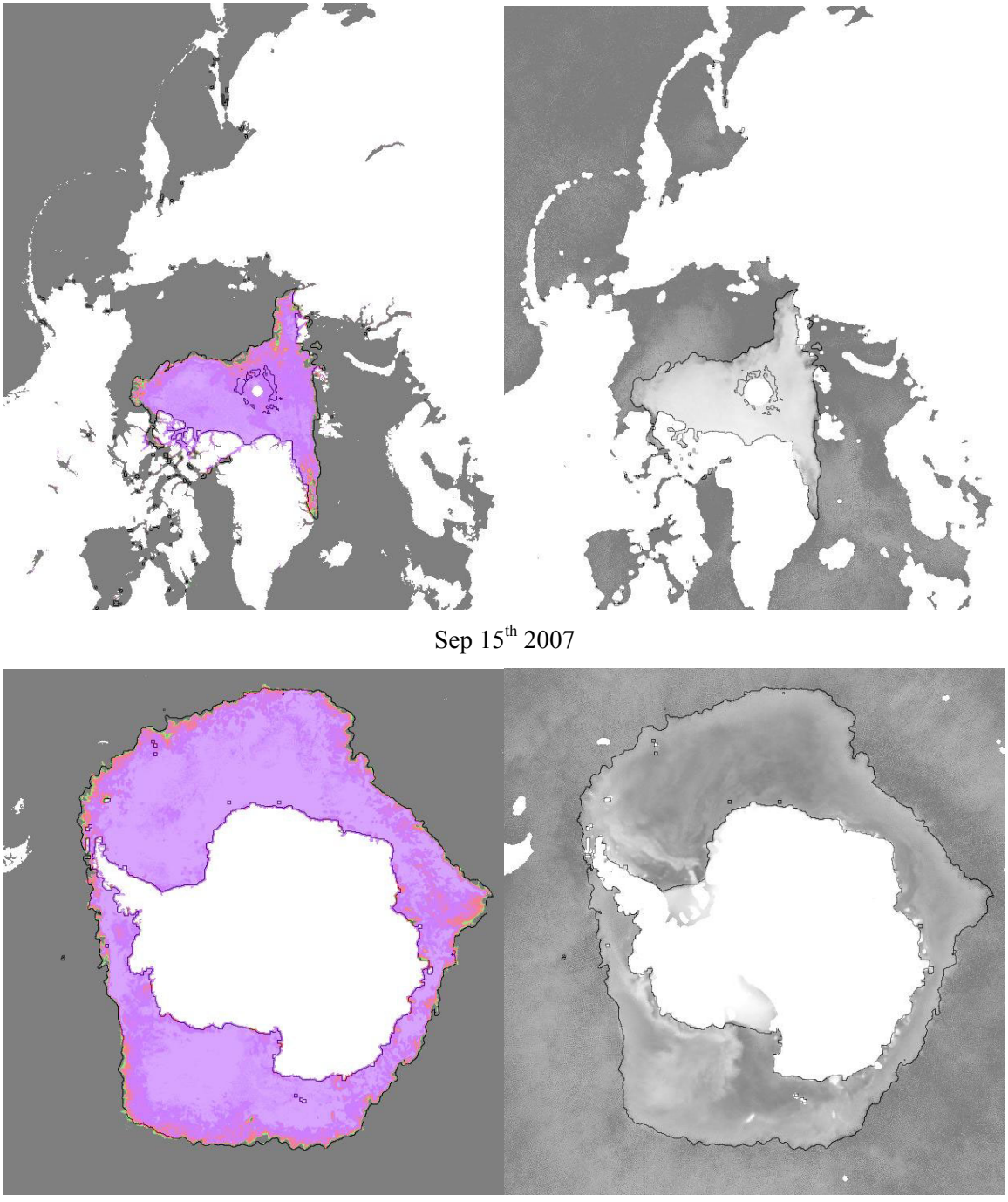

Figure 30 – QSCAT KNMI (1.0 dB) ice edge vs AMSR sea ice concentration (LEFT) and on QSCAT V-pol backscatter background (RIGHT)

6 Summary and recommendations

In this report, we lay out the groundwork for the implementation of a Near-Real Time sea ice detection algorithm using SeaWinds backscatter data. Well beyond the contrasts between sea ice and ocean backscatter properties exploited in earlier algorithms, the KNMI algorithm uses full geophysical model functions in the original SeaWinds measurement space to discriminate sea ice from water returns. The fitted Ku-band sea ice model for SeaWinds and its measurement noise characteristics are employed for sea ice detection using SeaWinds data. The normalized distances in the 4-D measurement space to the sea ice and ocean wind GMF manifolds given by MLE residuals are converted into sea ice and ocean wind conditional probabilities, and these are finally combined into a posterior probability using a Bayesian approach. Using the full GMFs for discriminating wind and sea ice in this way is proven to be effective. The performance of the SeaWinds KNMI algorithm is less noisy than the already existing SeaWinds BYU algorithm and adjusts better to the validating references available (AMSR-NT2 concentrations and sea ice charts from the US National Ice Center) during the freeze-up and winter periods. The performance of the algorithm during the spring and summer months (when the disagreement with AMSR NT2 is greatest) is difficult to validate due to lack of additional (independent) reference data, although the results appear consistent with US NIC charts, indicating substantial negative biases in AMSR NT2 sea ice extents.

- Emphasize (radiometer lead in growth season, radar lead in melt season, complementarity)
- Emphasize (4% agreement in sea ice extent with AMSR NT2 (15% concentration edge) during the growth season)
- Comment on ‘conservativeness’ of old BYU mask (good as effective ice mask) that suffers from noise and does not adjust to AMSR data as well as the new algorithm
- Compare against hi-res SCP QSCAT sea ice maps
- Show signature of rain
- Revise acronyms
- Attempt estimation of low concentration (0.4 – 1.0 dB algorithm difference) and correlate with AMSR [Haarpaintner,…]
- Mention iceberg tracking [Long, EOS], melt [Howell, IEEE] and classification [Nghiem, JGR]

Aspects to be further elaborated on include:

1) Improved methods for the Bayesian propagation (update) of prior sea ice probabilities.
2) The determination of sea ice concentrations (i.e. detection of mixed ice-water states) from conditional sea ice probabilities.

3) The creation of a historic record of QUIKSCAT sea ice extents (melt, classes and drifts) from archived data.

Appendices

Appendix A

Empirical Ku-Band Ocean GMF (*NSCAT2*)

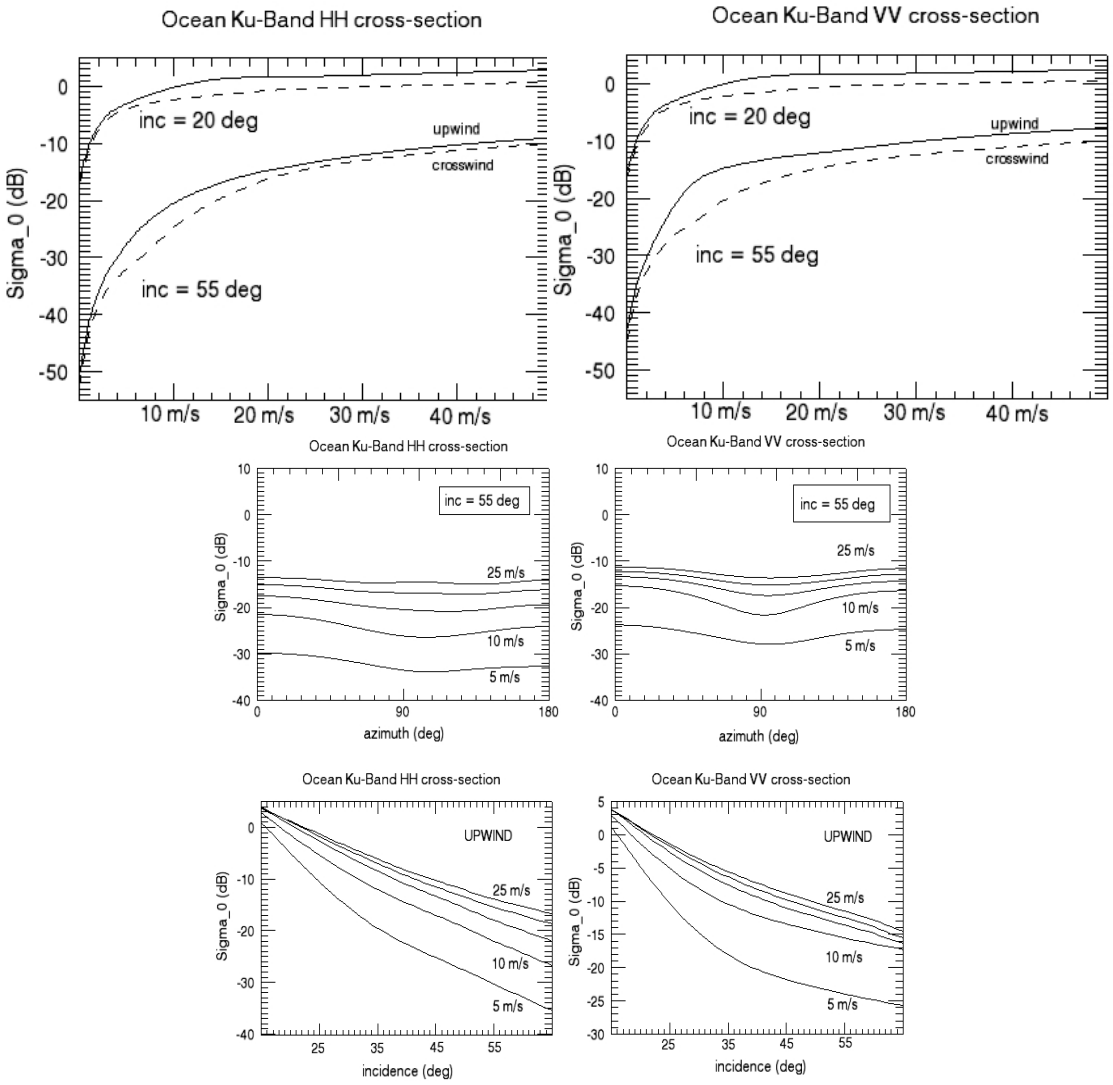

Figure A1 – Empirical Ku-Band GMF (a.k.a. NSCAT2)

Appendix B1

Linear fits to sea ice backscatter (using BYU masks) Arctic

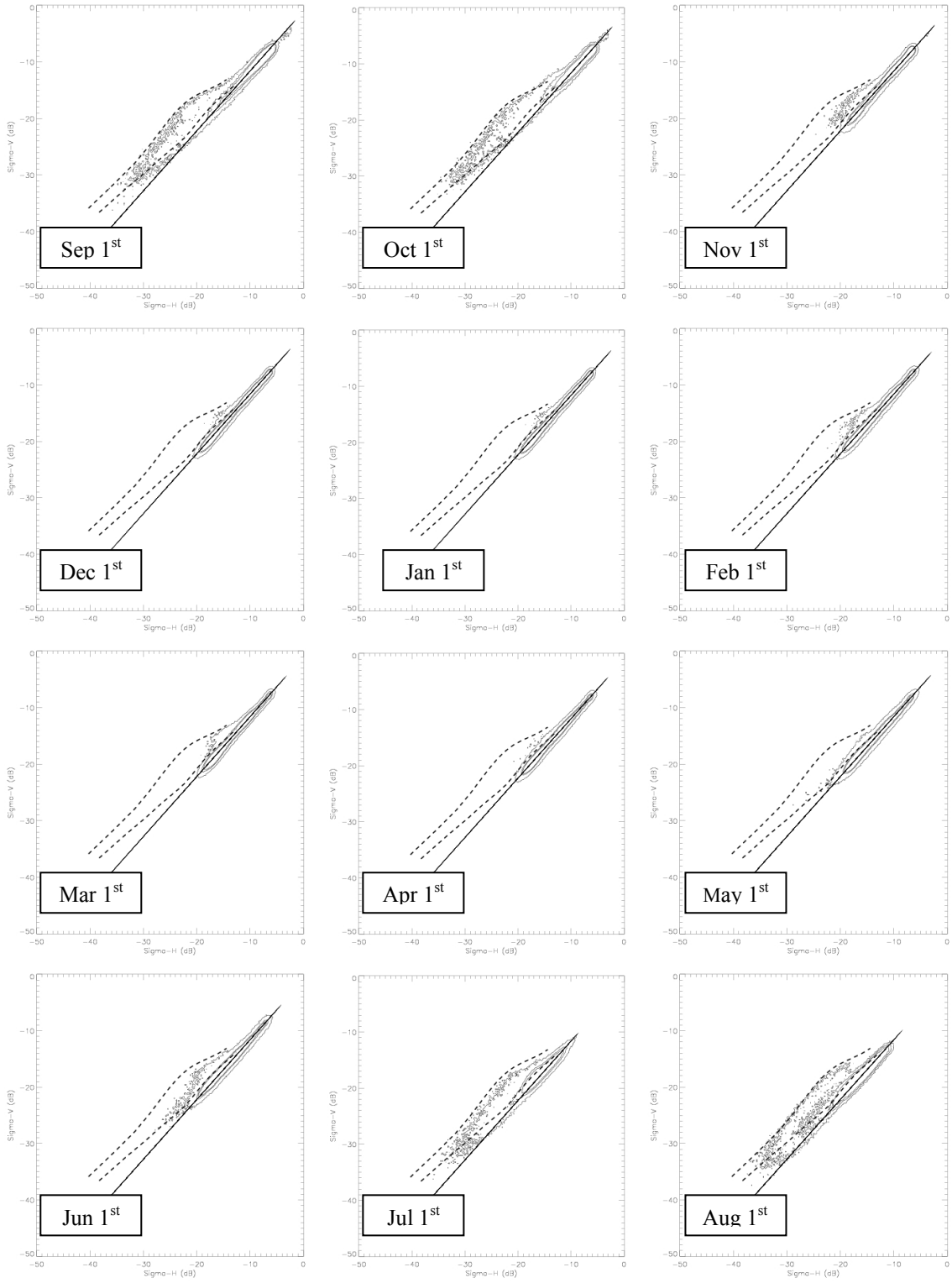

Appendix B2

Linear fits to sea ice backscatter (BYU masks) Antarctic

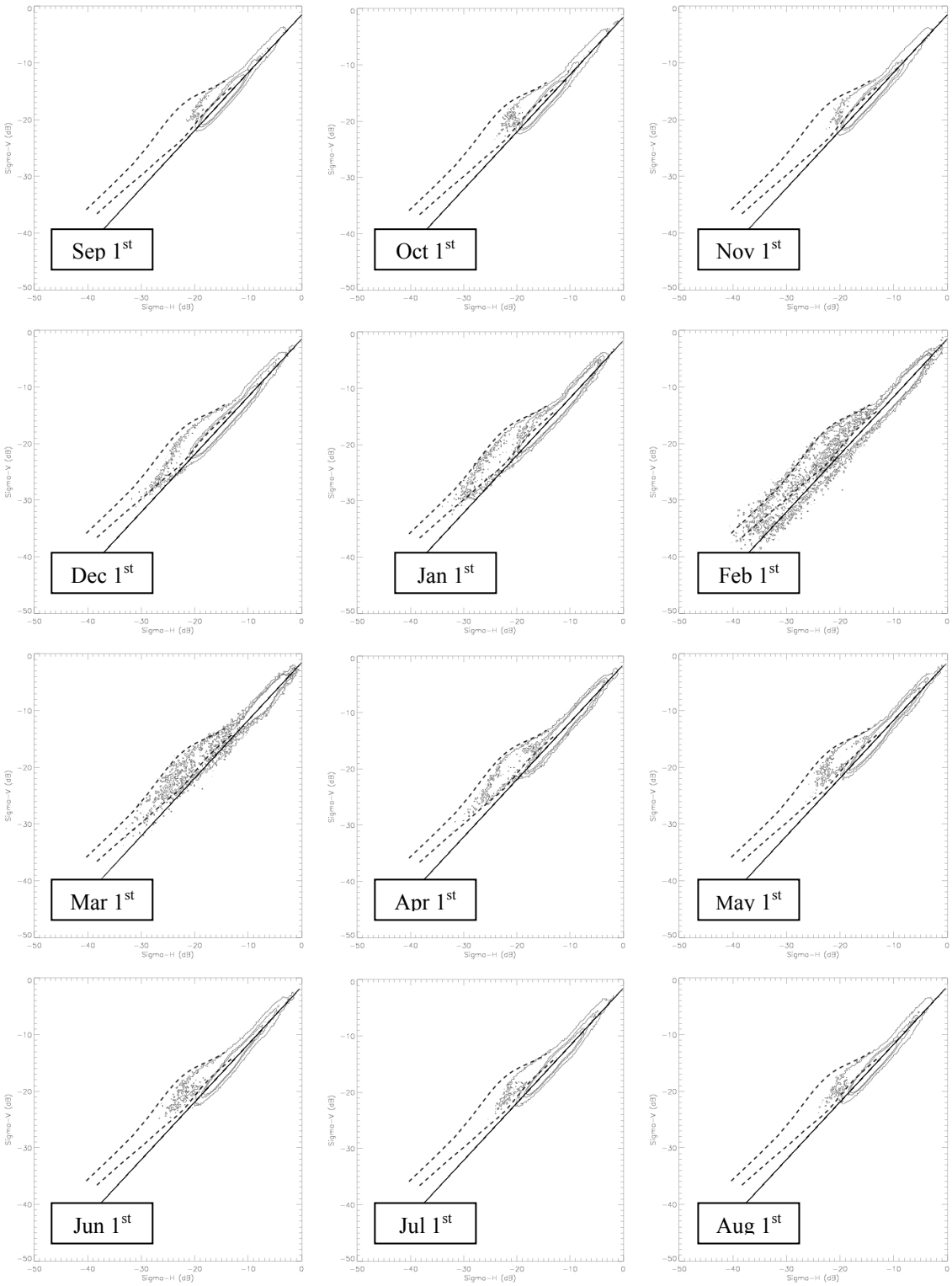

Appendix C1

Scatter distribution – Distances to linear ice model (in dB space)

Arctic

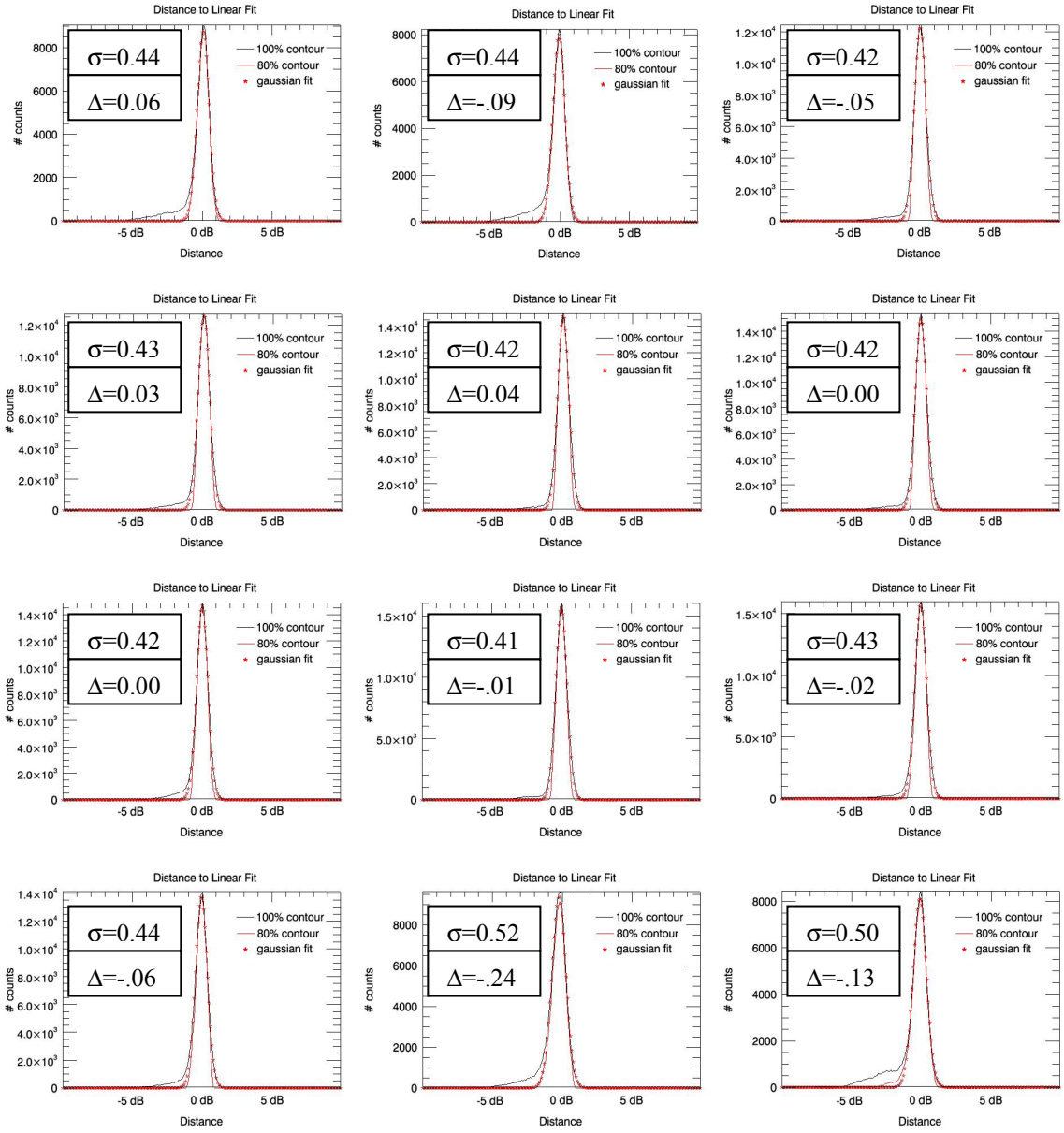

Appendix C2

Scatter distribution – Distances to linear ice model (in dB space)

Antarctic

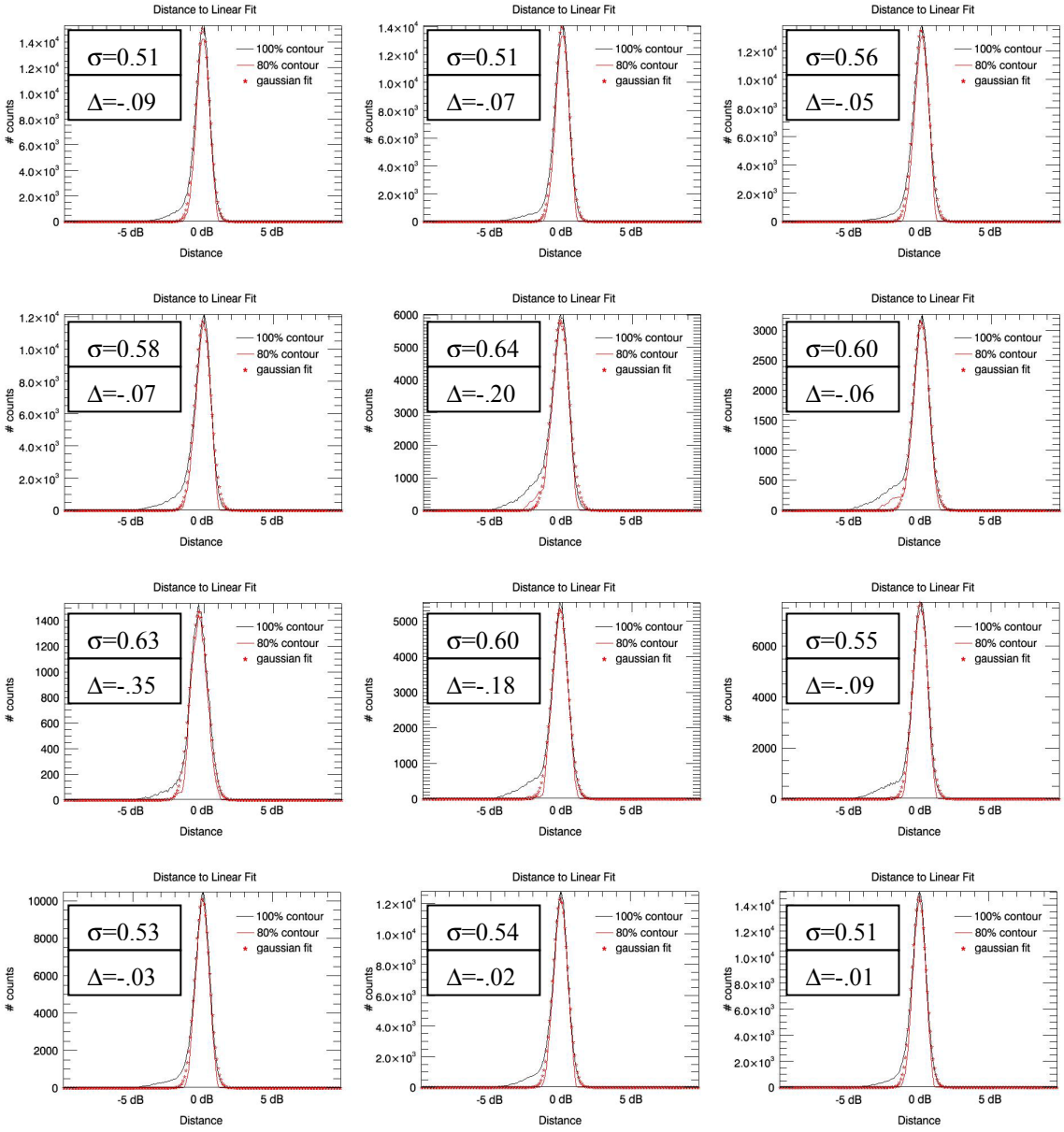

Appendix D1

AMSR (NT2, dark blue, +15% concentration) vs QUIKSCAT (BYU, light blue) sea ice masks – Arctic

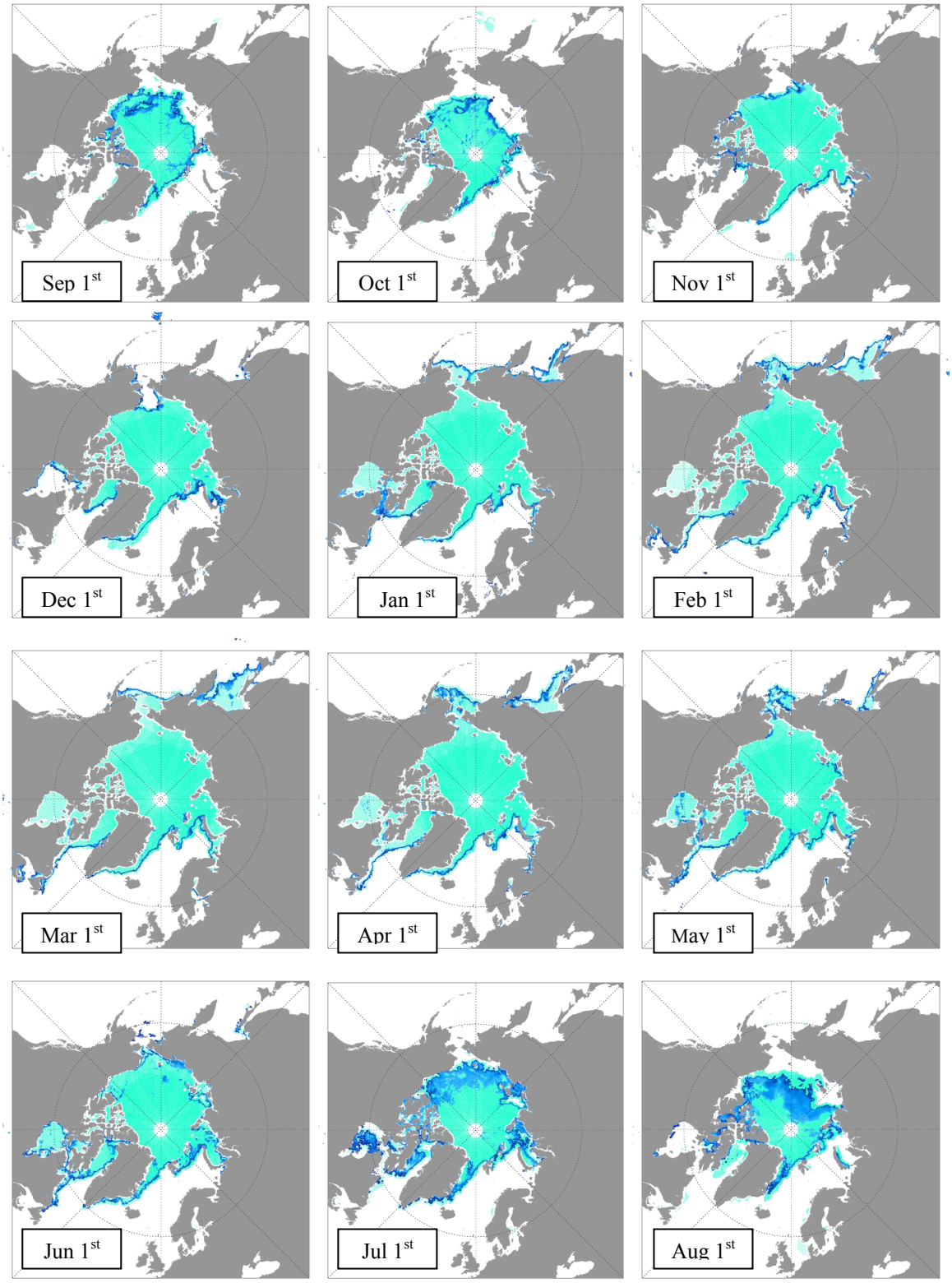

Appendix D2

AMSR (NT2, dark blue, +15% concentration) vs QUIKSCAT (BYU, light blue) sea ice masks – Antarctic

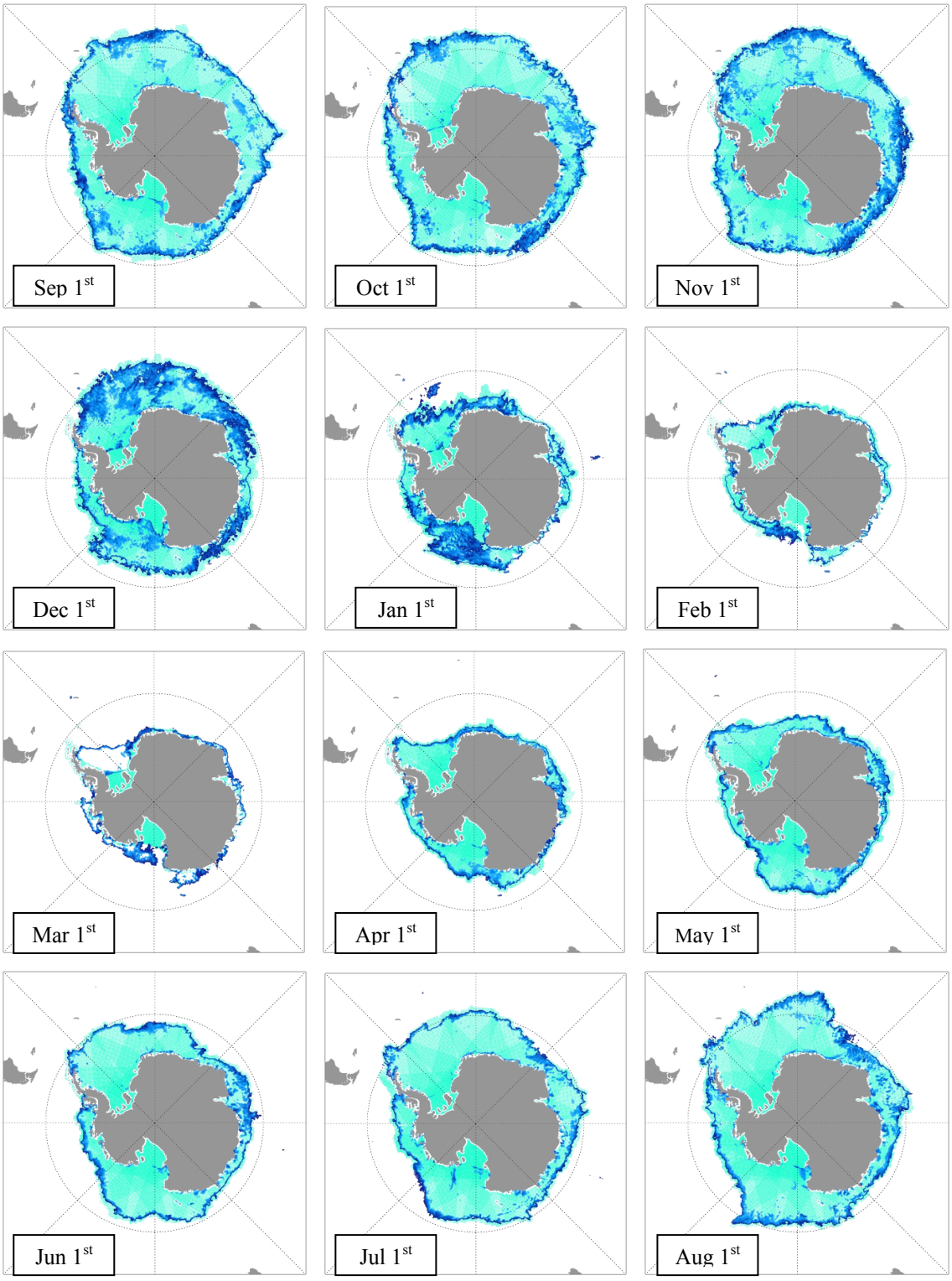

References

[Abreu, 2002] Abreu, R.D., Wilson, K., Arkett, M., Langlois, D., "Evaluating the use of QUIKSCAT data for operational sea ice monitoring", IEEE IGARSS, Vol.5, pp.3032 – 3033, 2002.

[Agnew, 2003] Agnew, T., Howell, S., "The use of operational ice charts for evaluating passive microwave ice concentration data", Atmosphere-Ocean 41 (4), 317-331, 2003.

[Anderson, 2005] Anderson, H.S., Long, D.G., "Sea ice mapping method for Seawinds", IEEE TGRS, Vol.43, No.3, 2005.

[Cavalieri, 2004] Cavalieri, D., and J. Comiso, "AMSR-E/Aqua Daily L3 12.5 km Tb, Sea Ice Conc., & Snow Depth Polar Grids V001", March to June 2004. Boulder, CO, USA: National Snow and Ice Data Center. Digital media, 2004.

[Cavalieri, 2006] Cavalieri, D.J., Markus, T., Hall, D.K., Gasiewski, A.J., Klein, M., Ivanoff, A., "Assessment of EOS Aqua AMSR-E Arctic sea ice concentrations using LANDSAT-7 and airborne microwave imagery", IEEE TGRS, Vol.44, No.11, 2006.

[Dedrick, 2001] Dedrick, K.R., Partington, K., VanWoert, M., Bertoia, C., Benner, D., "US National / Naval Ice Center digital sea ice and climatology data", Canadian Journal of Remote Sensing, Vol.27, No.5, 2001.

[Early, 1997] Early, D.S., Long, D.G., "Azimuthal modulation of C-Band scatterometer $\sigma 0$ over southern ocean sea ice", IEEE TGRS, Vol.35, No.5, 1997.

[Ezraty, 2001] Ezraty, R., Piolle, J.F., "Seawinds on Polar Sea Ice Grids: User Manual", CONVECTION Report No.5, 2001.

[Fernandez, 2006] Fernandez, D.E., Carswell, J.R., Frasier, S., Chang, P.S., Black, P.G., Marks, F.D., "Dual-polarized C- and Ku-band backscatter response to hurricane-force winds", JGR, Vol.111, C08013, 2006.

[Gohin, 1994] Gohin, F., Cavanie, A., “A first try at identification of sea ice using the three beam scatterometer of ERS-1”, Int. J. Remote Sensing, Vol.15, No.6, pp 1221-1228, 1994.

[de Haan, 2001] de Haan, S., Stoffelen, A., “Ice discrimination using ERS scatterometer”, OSI SAF Document KNMI-TEC-TN-120, EUMETSAT, 2001.

[Haarpaintner, 2004] Haarpaintner, J., Tonboe, R., Long, D., Van Woert, M.L., “Automatic detection and validity of the sea ice edge: an application of enhanced resolution QUIKSCAT/SeaWinds data”, IEEE TGRS, Vol.42, No.7, 2004.

[Heinrichs, 2006] Heinrichs, J.F., Cavalieri, D.J., Markus, T., “Assessment of the AMSR sea ice concentration product at the ice edge using RADARSAT-1 and MODIS imagery”, IEEE TGRS, Vol.44, No.11, 2006.

[Johnson, 1994] Johnson, N.L., Kotz, S., Balakrishnan, N., “Continuous univariate distributions”, Wiley, New York, 1994.

[Jones, 1977] Jones, W.L., Schroeder, L.C., Mitchell, J.L., “Aircraft measurements of the microwave scattering signature of the ocean”, IEEE Antennas & Propagation, Vol.25, No.1, 1977.

[de Kloe, 2007] de Kloe, J., Portabella, M., Stoffelen, A., Verhoef, A., Verspeek, J., Vogelzang, J., “SDP User Manual and Reference Guide”, NWP SAF Document KN-UD-002, EUMETSAT, 2007

[Leidner, 2000] Leidner, S.M., Hoffman, R.N., Augenbaum, J., “Seawinds Scatterometer real-time BUFR geophysical product”, NOAA/NESDIS, 2000.

[Markus, 2000] Markus, T., Cavalieri, D., “An enhancement of the NASA Team sea ice algorithm”, IEEE TGRS, 38: 1387-1398, 2000.

[Markus, 2002] Markus, T., Dokken, S., “Evaluation of late summer passive microwave Arctic sea ice retrievals”, IEEE TGRS, Vol.40, No.2, 2002.

[Meier, 2005] Meier, W.N., “A comparison of passive microwave ice concentration algorithm retrievals with AVHRR imagery in Arctic peripheral seas”, IEEE TGRS, Vol.43, No.6, 2005.

[Meier, 2006] Meier, W.N., Fetterer, F., Fowler, C., Clemente-Colon, P., Street, T., “Operational sea ice charts: an integrated data product suitable for observing long term changes in Artic sea ice?”, AGU Fall Meeting, 2006.

[Meier, 2008] Meier, W.N., Stroeve, J., “Comparison of sea ice extent and ice-edge location estimates from passive microwave and enhanced resolution scatterometer data”, Ann. Glaciology, No.48, 2008.

[Onstott, 1987] Onstott, R.G., Grenfell, T.C., Matzler, C., Luther, C.A., Svendsen, E.A., “Evolution of microwave sea ice signatures during early summer and midsummer in the Marginal Ice Zone”, JGR, Vol.92, No.C7, 1987.

[Portabella, 2006] Portabella, M., Stoffelen, A., “Scatterometer backscatter uncertainty due to wind variability”, IEEE TGRS, Vol.44, No.11, 2006.

[Remund, 1998] Remund, Q.P., Long, D.G., “Sea ice mapping algorithm for QuikSCAT and Seawinds”, IEEE IGARSS, pp. 1686-1688, 1998

[Remund, 1999] Remund, Q.P., Long, D.G., “Sea ice extent mapping using Ku-band scatterometer data”, JGR, Vol.104, No.C5, pp 11,515-11,527, 1999.

[Remund, 2000] Remund, Q.P., Long, D.G., “Iterative estimation of Antarctic sea ice extent using Seawinds data”, IEEE IGARSS, pp. 491-493, 2000.

[Remund, 2003] Remund, Q.P., Long, D.G., “Large scale inverse Ku-Band backscatter modeling of sea ice”, IEEE TGRS, Vol.41, No.8, 2003.

[Spencer, 2000] Spencer, M.K., Chianlin, W., Long, D.G., “Improved resolution backscatter measurements with the Seawinds pencil-beam scatterometer”, IEEE TGRS, Vol.38, No.1, 2000.

[Stoffelen, 2006] Stoffelen, A., Portabella, M., “On bayesian scatterometer wind inversion”, IEEE TGRS, Vol.44, No.6, 2006.

[Verspeek, 2006] Verspeek, J.A., “Sea ice classification using Bayesian statistics”, KNMI Internal Report, 2006.

[Wentz, 1999] Wentz, F.J., Smith, D.K., “A model function for the normalized radar cross-section at 14GHz derived from NSCAT observations”, JGR, Vol.104, N.C5, pp. 11499-11514, 1999.

[Yueh, 1997] Yueh, S.H., Kwok, R., Lou, S.H., Tsai, W.Y., “Sea ice identification using dual polarized Ku-Band data”, IEEE TGRS, Vol.35, No.3, 1997.

Acknowledgements

We acknowledge the help and collaboration of our colleagues working at KNMI, and more in particular the people in the scatterometer group. This work is funded by the European Meteorological Satellite Organization (EUMETSAT) Ocean & Sea Ice (OSI) Satellite Application Facilities (SAF).